Energy Science & Engineering

ORIGINAL ARTICLE OPEN ACCESS

Feed-Forward PID-Based Cooperative Control Strategy for Air Mass Flow and Pressure in PEMFC Systems

Xinhao Bian[1,2,3] | Gang Chen[4] | Na Li[5] | Liang Tong[1,2,3] | Rui Yang[6] | Boyang Shen[7]

[1]State Key Laboratory of Maritime Technology and Safety, Wuhan University of Technology, Wuhan, Hubei, China | [2]National Engineering Research Center for Water Transport Safety, Wuhan University of Technology, Wuhan, Hubei, China | [3]Reliability Engineering Institute, School of Transportation and Logistics Engineering, Wuhan University of Technology, Wuhan, Hubei, China | [4]School of Naval Architecture Ocean and Energy Power Engineering, Wuhan University of Technology, Wuhan, Hubei, China | [5]Hubei Huazhong Electric Power Technology Development Co., Ltd, Wuhan, Hubei, China | [6]China Water Transport Research Institute, Beijing, China | [7]Department of Engineering, University of Cambridge, Cambridge, UK

Correspondence: Gang Chen (chen_gang@whut.edu.cn) | Liang Tong (tongliang2@whut.edu.cn)

Received: 18 February 2025 | **Revised:** 24 June 2025 | **Accepted:** 3 July 2025

Funding: This study is Supported by the National Natural Science Foundation of China (Grants U23A20680), Jiangsu Province Carbon Peaking and Carbon Neutrality Science, Technology Innovation Special Fund (Industry Foresight and Key Technology Core Research) Project (BE2023091-2), Provincial Science and Technology Innovation Strategy Special Project of Shaoguan City (230317166277914), Special Program for Science and Technology Innovation in Industrial Bases (2023010402010790).

Keywords: air mass flow rate and pressure | feed-forward PID control | proton exchange membrane fuel cell | synergistic control

ABSTRACT

The air supply system is regarded as a critical component in high-power proton exchange membrane fuel cells (PEMFCs). Precise control of air mass flow rate and pressure is essential for improving system efficiency, durability, and output power stability. In this study, an 86 kW-grade PEMFC engine was designed, and a feed-forward PID-based control strategy was developed, which achieves dynamic air pressure-flow decoupling of the PEMFC and provides a quicker response to radically varying loads. Experiments were conducted under various load conditions to evaluate the system's performance. The results demonstrated that the proposed strategy achieved a short transient response time and stable tracking of air mass flow and cathode inlet pressure. Additionally, the voltage deviation between the minimum and average values of individual cells was maintained below 0.05 V, indicating excellent uniformity within the stack. This uniformity ensures the long-term durability and reliability of the fuel cell stack.

1 | Introduction

Energy and environmental sustainability are among the most pressing challenges facing society today. The efficient utilisation of clean energy is crucial for achieving sustainable development. The global energy demand is increasing at a rate of 1.3% per year, while fossil fuels dominate the energy sector and are the primary source of greenhouse gas emissions [1, 2]. Renewable energy resources have been considered as a feasible solution for reducing greenhouse gas emissions. Nevertheless, most renewable energy sources exhibit inherent intermittency, uncertainty, and randomness and geographic constraints, leading to significant spatiotemporal mismatches between energy generation patterns and end-user demand. To address these critical challenges, the strategic implementation of advanced energy conversion technologies within power grid infrastructures becomes imperative [3]. Hydrogen energy has emerged as a pivotal component in the global transition to clean energy systems, offering a viable solution for achieving large-scale deep decarbonisation across multiple sectors. The electrolysis of water to produce green hydrogen represents not only a sustainable method for hydrogen generation but also provides an effective strategy for mitigating the inherent intermittency and variability challenges associated with renewable energy

sources [4]. However, most renewable energy sources are intermittent and geographically constrained, resulting in temporal and spatial gaps between the energy availability and the consumption of the end-users. To tackle these problems, it is necessary to deploy appropriate energy conversion devices for power grids. Fuel cells serve as highly efficient energy conversion devices, playing a pivotal role in enabling the practical utilisation of hydrogen energy. In response, renewable energy and hydrogen fuel cells have become important research directions for addressing the escalating environmental contamination and global climate change caused by greenhouse gases [5]. Fuel cell power generation systems offer several advantages, including high efficiency, environmental friendliness, low noise, rapid startup, and high system integration [6]. These systems are increasingly applied in various fields, such as the automotive, marine, and aerospace industries. With this trend comes a growing demand for higher-output fuel cell systems. However, increasing the power output of fuel cells leads to higher fuel consumption and imposes more stringent requirements on the fuel supply system. The air supply system, in particular, plays a critical role in ensuring the proper air flow and pressure, which are essential to prevent membrane damage from fuel starvation or excessive pressure. The commercialisation of proton exchange membrane fuel cells (PEMFCs) is still hindered by their limited-service life. During extended operation, PEMFC performance progressively degrades owing to complex operating conditions and component aging, eventually reaching the minimum acceptable performance threshold [7]. The performance degradation primarily originates from multiple complex mechanisms, notably electrochemical deterioration of electrode materials, catalyst dissolution and aggregation, mechanical failure in membrane electrode assemblies, and instability of operating parameters [8]. Thus, it supports the stable operation of auxiliary components, thereby enhancing the longevity of the fuel cell stack and improving the net system power [9–11]. Given these challenges, there has been significant interest in developing advanced control strategies for the gas supply system of PEMFC.

Kuo et al. [12] proposed a fuzzy proportional-integral (PI) controller aimed at regulating the hydrogen supply flow rate to enhance the system's output power and reduce the oxygen excess ratio (OER) on the hydrogen supply side. Ye et al. [13] developed a control strategy based on the proportional-integral-derivative (PID) algorithm, explicitly tailored for high-power fuel cell systems' air supply system components. Shen et al. [14] introduced a neural network-based rectified PID control algorithm. Simulation results indicated that this algorithm reduces OER overshoot by ~30% compared to conventional PID controllers while achieving faster and more efficient voltage regulation. However, this algorithm has not been implemented in actual controllers and lacks experimental validation. Baroud et al. [15] proposed a novel hybrid fuzzy PID controller for gas supply management in PEMFC systems, demonstrating the superiority of this control scheme through experimental results. Pan et al. [16] investigated both traditional PID and Multiple PID (M-PID) control methods. Their experimental findings showed that while both algorithms satisfy the system's operational requirements under various conditions, the M-PID algorithm enables superior system performance. Besides, Routh et al. [17] proposed designed a fractional-order PI/D (FOPID) controller for the cathode-side pressure regulation problem of PEMFC, and concluded that the pressure management method based on the fractional-order model and controller is the most effective. Besides, the FOPID controller for PEMFC based on genetic algorithm is also proposed in ref. [18]. The results indicated that the FOPID control method was characterised by small overshoot and high stability. And the PEMFC operating efficiency is improved by 2%.

In addition to classical PID-based control methods, more advanced control algorithms have been developed for air supply systems in PEMFCs. Han et al. [19] proposed a model reference adaptive control (MRAC) algorithm for airflow management, addressing surge issues by establishing a compressor surge prediction model. Their simulation results demonstrate that MRAC outperforms traditional feedback control methods regarding overall performance. Chuang et al. [20] introduced a flow control strategy for PEMFCs based on the theory of inventive problem solving and game theory. They constructed a simulation model to regulate inlet temperature, pressure, and air and hydrogen flow rates. The results indicate that this strategy significantly enhances outlet temperature and pressure and reduces pressure drops. Pilloni et al. [21] proposed a sliding mode control approach for output feedback control in PEMFC systems, focusing on regulating the air mass flow rate to maintain an optimal OER by controlling the air supply. A study [22] explored the analogy between cascade and air supply systems, proposing a cascade controller based on uncertainty perturbation estimation and the Lyapunov method. The efficacy of this approach was validated experimentally. Wang et al. [23] developed a second-order active disturbance rejection control algorithm, targeting the optimal OER parameter for control purposes. Simulation results suggest that this algorithm can enhance both the net power output and the efficiency of PEMFC systems. Moreover, a second-order linear active disturbance rejection control self-tuning control strategy for PEMFC based on parameter identification results was proposed in [24]. Simulation results indicate that the proposed control strategy could significantly improve the voltage stability and system efficiency under dynamic conditions resulting in a system dynamic response time of no more than 0.1 s. Besides, Fang et al. [25] proposed a nonsingular terminal sliding mode controller based on a sliding mode observer. The results show that this controller improves the response speed by 63% over the terminal sliding mode structure, which effectively improves the efficiency and stability of the PEMFC system.

In the studies mentioned above on OER control, the state variables related to OER are often derived directly from mathematical models within a simulation environment. However, in real-world applications, many variables could be more complex or costly to measure directly. As a result, it is necessary to employ algorithms that can estimate these variables indirectly. Thus, Wang et al. [26] proposed a discrete neural network OER control strategy incorporating an observer. They utilised Lyapunov stability theory to demonstrate that the system's tracking error is semi-globally consistent and uniformly bounded. The efficacy and superiority of the proposed controller were confirmed through hardware-in-the-loop (HIL) testing and numerical modelling. Deng et al. [27] developed an OER controller based on a higher-order sliding-mode state observer.

Experimental results showed that this controller is both viable and effective compared to traditional controllers. Wei et al. [28] introduced a coordinated control strategy combining input-output linearisation with a sliding mode approach to regulate OER and air pressure. Simulation results indicated that the proposed controller accelerates OER regulation by ~50%, reduces cathode pressure overshoot by 15%, and significantly enhances the dynamic response of stack voltage and net power. Eli et al. [29] proposed a multi-input, multi-output controller to control fuel cell air paths precisely. Experimental and simulation results validated that this control method effectively reduces hydrogen fuel consumption in PEMFCs.

The above studies have focused on controlling fuel cell air flow using classical and modern control theories, primarily through simulations or experiments. However, research specifically addressing the impact of air pressure on fuel cell performance still needs to be completed. Zhao et al. [30] designed a fuzzy PID air flow pressure decoupling controller. Step load tests demonstrated that the fuzzy PID control outperforms traditional PID decoupling control regarding regulation time, overshoot, and steady-state error. Chen et al. [31] employed an internal model decoupling control strategy to address air flow and intake pressure coupling. Their simulation results demonstrated the effectiveness of the internal model decoupling controller in achieving the separation of air pressure and flow. Song et al. [32] applied the active disturbance rejection decoupling control principle to a strongly coupled system, designing a dynamic decoupling controller for flow and pressure. The simulation results indicated that this controller significantly reduces the flow-pressure coupling effect, thereby enhancing stack performance by minimising flow and pressure disturbances. Li et al. [33] developed a super-twist sliding mode controller to regulate cathode flow and pressure and proposed a method for system parameter identification and fine-tuning of controller parameters. This approach effectively managed the cathode conditions, contributing to more stable and efficient fuel cell operation.

Currently, most research efforts focus on controlling the OER. For high-power PEMFC systems, however, achieving the synergistic regulation of pressure and air flow is a crucial problem that must be resolved. More research needs to be done on the synergistic regulation of pressure and flow, and most are still in the simulation stage. Sun et al. [34] proposed a coordinated control strategy for the hydrogen supply systems based on feed-forward and internal mode decoupling control to realise the independent control of air flow and pressure for improving the efficiency of centrifugal air compressors. Wang et al. [35] used an active differential pressure regulation-based approach to enhance the performance of flow control valves using a nonlinear flow correction strategy, which can compensate for changes in flow rate by controlling the differential pressure, thus achieving an arbitrarily shaped target flow profile within the differential pressure control range. However, the study only controls the flow control of the valve without considering the control of pressure. Zhao et al. [36] designed a PEMFC hydrogen supply system based on the cyclic mode. The proposed control strategy uses a PI controller to control the proportional valve to adjust the difference between the anode pressure and the actual anode pressure so that the hydrogen volume fraction is kept under 6% and the hydrogen excess rate is not more than 1.5. The anode pressure is relatively stable under the middle and high operating conditions. However, the control object of this control strategy is mainly the hydrogen supply system pressure, excluding the flow rate.

To address the abovementioned gaps, Yin et al. [37] proposed a sliding mode nonlinear control method based on adaptive super twisting to realise the synergistic control of air and hydrogen supply. The performance of this control method was verified by two simulation scenarios to effectively regulate the oxygen excess ratio, hydrogen excess ratio and the pressure difference between two sides of the membrane. However, the reliability and safety of the method were not verified in a real hydrogen fuel cell device. Li et al. [38] designed a nonlinear controller based on the feedback technique for the cooperative control of pressure and airflow. The test rig was built using a positive displacement compressor for airflow control, and a simple proportional-integral control with feedforward compensation was used to regulate the airflow. However, since a centrifugal compressor was not used, the pressure-force coupling dynamics needed to be accounted for. Existing research on the synergistic control of pressure and flow in gas supply systems has primarily been validated through simulations, with some experiments conducted on small fuel cell stacks. Consequently, the current experimental results need to be more robust to effectively demonstrate the viability of coordinated control strategies in large vehicles equipped with centrifugal compressors.

The feed-forward PID control strategy combines integral anti-saturation, pressure deviation deadband, and actuator output limitation to calculate the deviation and rate of change of air mass flow and pressure [39]. The control strategy could respond to the dynamic changes of the system quicker and more accurately than the fuzzy-PID strategy [40]. Thus, this manuscript proposes an enhanced feed-forward dual-loop segmented PID controller for the air supply system. This controller is designed to account for the reciprocal effects of pressure and air mass flow on fuel cell system operation and overall system power output stability and safety. The proposed controller was implemented in an 86 kW fuel cell engine, and its performance was analysed under various operating conditions. Experimental results demonstrate the controller's effectiveness in accurately achieving the desired flow and pressure levels.

The structure of this manuscript is organised as follows: Section 2 provides an overview of the fuel cell system and its modelling, details the controller design methodology, and outlines the control logic. Section 3 describes the process for selecting reference operating condition points, details the test bench setup, and outlines the experimental procedures. Section 4 presents and discusses the experimental results. Finally, Section 5 summarises the conclusions drawn from the study.

2 | Fuel Cell Systems and Controllers

2.1 | Fuel Cell System Architecture

This manuscript utilised an 86 kW PEMFC engine as the experimental subject. The front and right views of PEMFC engine are illustrated in Figure 1a,b, respectively. Figure 1c depicts the fuel cell system's architecture. The engine comprises several key

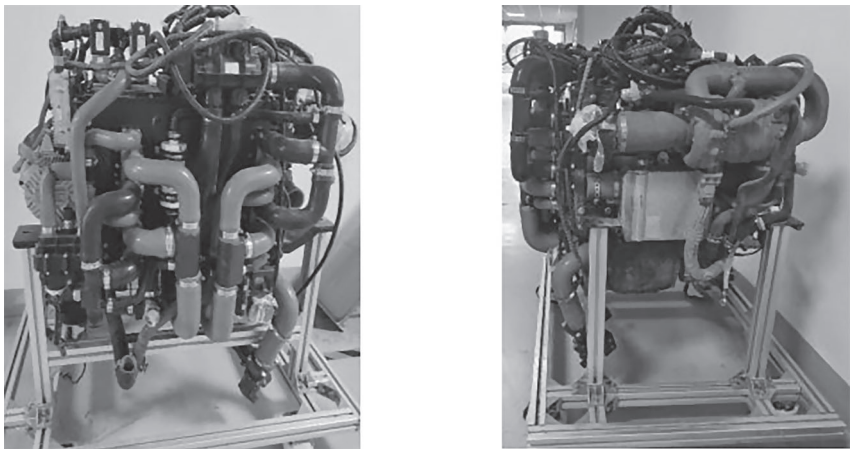

(a) (b)

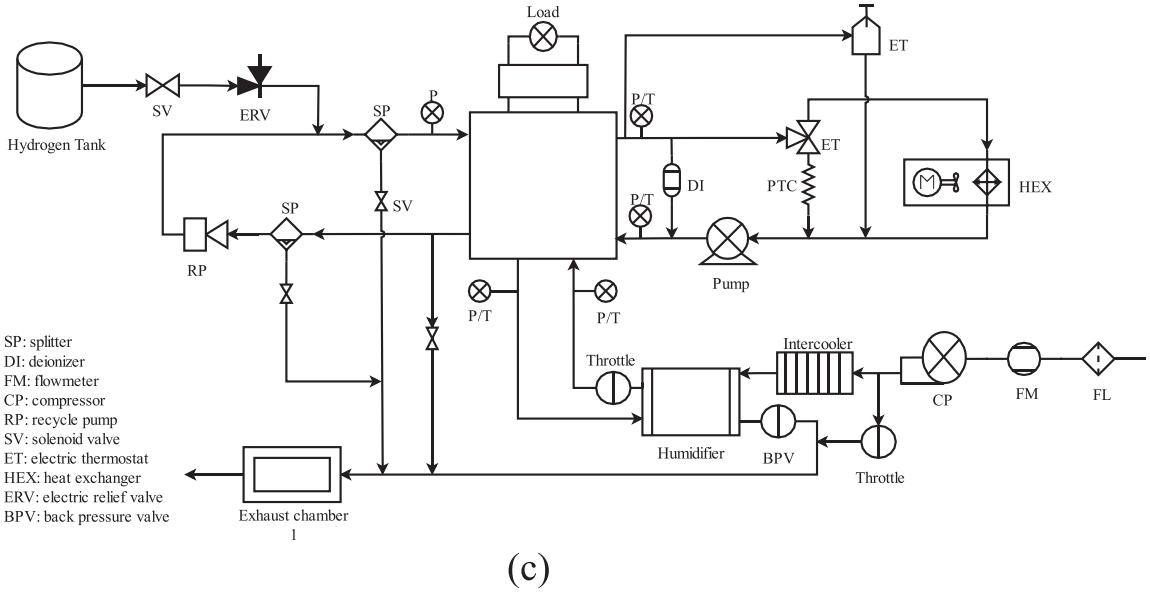

(c)

FIGURE 1 | PEMFC system architecture. (a) Front view of PEMFC engine. (b) Right view of PEMFC engine. (c) PEMFC system architecture.

TABLE 1 | Basic parameters of the fuel cell stack.

Parameters	Values	Parameters	Values
Number of single cells	370	Current range	0–500 (A)
Connection method	Series	Rated power	96 (kW)
Cooling method	Water cooling	Peak Power	105 (kW)
Voltage range	225–350 (V)	Polar plate area	260 (cm^2)

components, including the stack module, power electronic system, controller, hydrothermal management system, air supply system, and hydrogen supply system.

The air supply system comprised a centrifugal air compressor, a humidifier, an intercooler, and a backpressure valve. In the hydrogen subsystem, solenoid and pressure relief valves were employed to regulate the flow and pressure of high-pressure hydrogen. Additionally, an ejector and circulation pump were used to manage the supply of depressurised hydrogen, control circulation, and maintain the pressure differential between the anode and cathode within a specified range. Auxiliary components included a vapour separator, purge valve, and other parts.

The thermal management system comprised a circulating water pump, deionised water, a heat exchanger, and an electronic thermostat. The power electronics system included a bidirectional electronic load and a DC/DC converter to manage energy consumption and power delivery. Table 1 provides the basic parameters of the fuel cell stack.

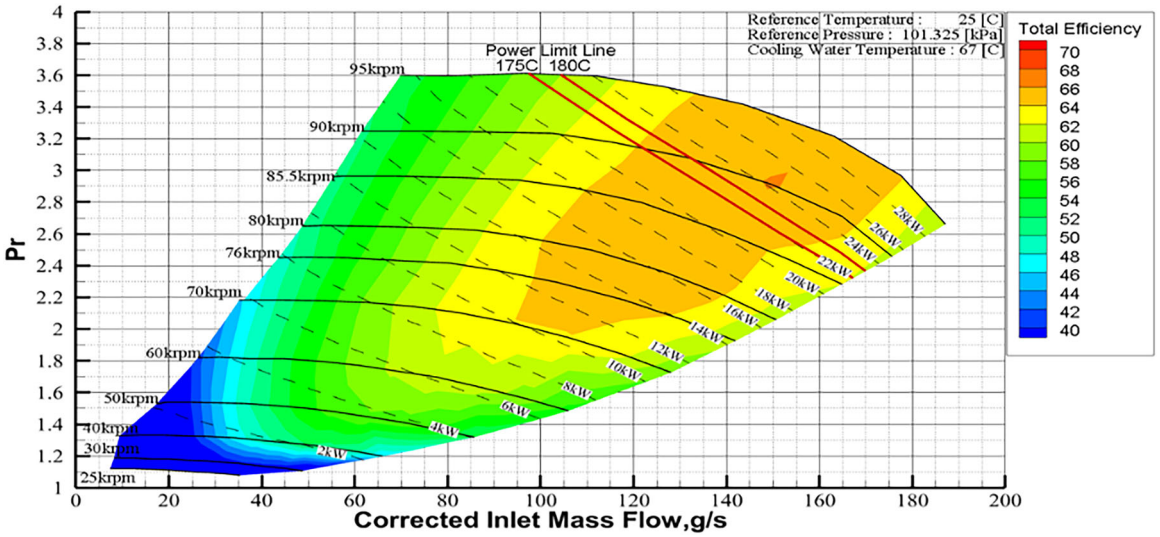

FIGURE 2 | Diagram of compressor performance's map.

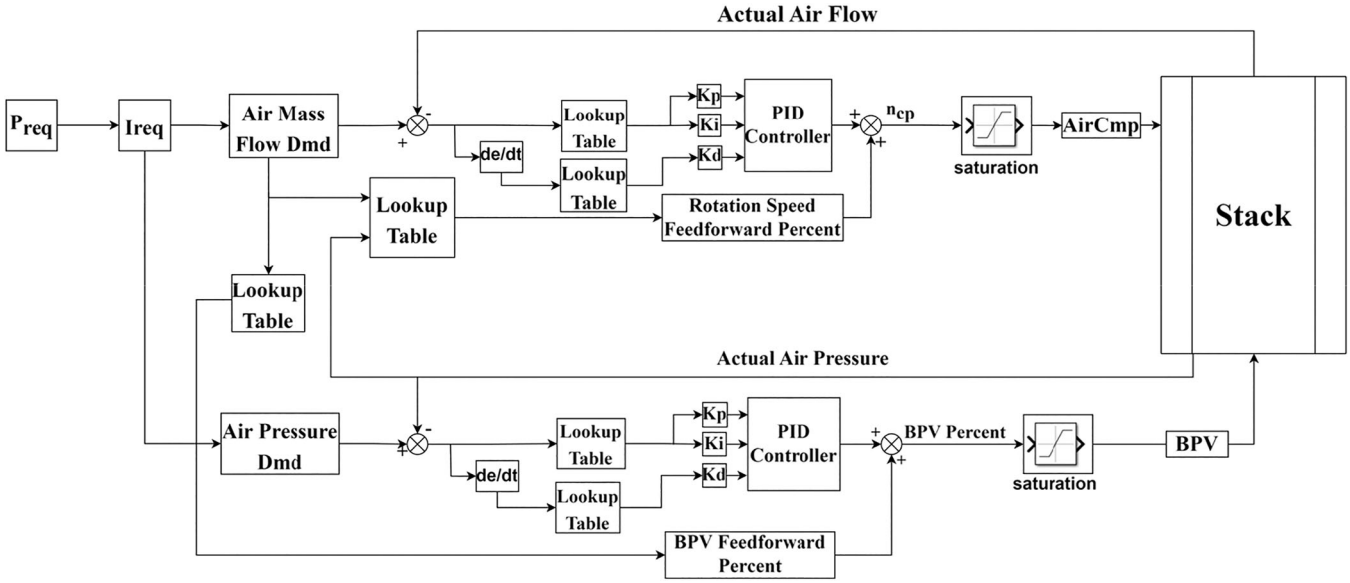

FIGURE 3 | Schematic diagram of feed-forward double-loop PID control logic.

TABLE 2 | PID control parameters.

Difference between actual and reference air mass flow rate values (L/min)	Air compressor			Difference between actual and reference air pressure (kPa)	Backpressure valve		
	K_p	K_i	K_d		K_p	K_i	K_d
−500	0.003	0.01	0	−10	0.8	0.2	0
−300	0.002	0.01	0	−5	0.6	0.15	0
−100	0.002	0.01	0	−3	0.5	0.1	0
−50	0	0.01	0	−1	0	0.05	0
0	0	0.01	0	0	0	0.05	0
50	0	0.01	0	1	0	0.05	0
100	0.002	0.01	0	3	0.2	0.05	0
300	0.002	0.01	0	5	0.3	0.08	0
500	0.003	0.01	0	10	0.5	0.1	0

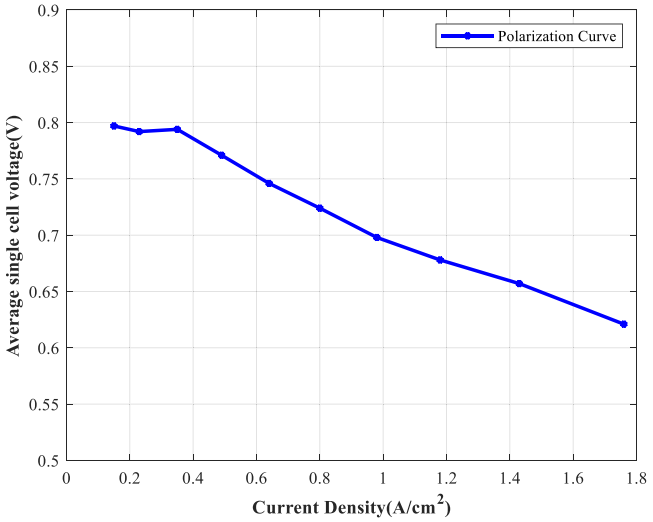

FIGURE 4 | Corresponding curves of a single cell's current density and average voltage.

2.2 | Modelling of Air Supply Systems

Based on the working characteristics of critical components in the air supply system, dynamic models for the air compressor, the supply and exhaust pipelines, and static models for the air humidifier and intercooler were developed. These models were established using the ideal gas law, the fluid continuity equation, and mechanisms describing the impact of pressure drops at the pipeline inlets and outlets on the gas state.

2.2.1 | Air Compressor Model

The air compressor model is divided into two components. The first component involves the compressor performance map, which determines the air flow rate through the compressor. The second component calculates the compressor speed based on the inertia of the motor and the compressor. The mass flow rate of the air discharged from the compressor is determined using the flow-pressure ratio-speed map diagram, which is derived from data associated with a two-stage supercharged, oil-free centrifugal air compressor used in an 86 kW class commercial fuel cell engine, as illustrated in Figure 2.

The compressor efficiency is derived from the static map using the compressor's mass flow rate and pressure ratio. Equation (1) calculates the temperature of the air exiting the compressor, while Equation (2) determines the pressure at the compressor's outlet.

$$\begin{aligned} T_{\mathrm{cp,out}} &= T_{\mathrm{cp,in}} + \frac{T_{\mathrm{cp,in}}}{\eta_{\mathrm{cp}}}\left[\left(\frac{P_{\mathrm{cp,out}}}{P_{\mathrm{cp,in}}}\right)^{\frac{\gamma-1}{\gamma}} - 1\right] \\ &= T_{atm} + \frac{T_{atm}}{\eta_{\mathrm{cp}}}\left[\left(\frac{P_{\mathrm{cp,out}}}{P_{\mathrm{cp,in}}}\right)^{\frac{\gamma-1}{\gamma}} - 1\right] \end{aligned} \tag{1}$$

$$P_{\mathrm{comp}} = \frac{C_{\mathrm{air}} \cdot T_{\mathrm{cp,in}}}{\eta_{\mathrm{cp}}}\left[\left(\frac{P_{\mathrm{cp,out}}}{P_{\mathrm{cp,out}}}\right)^{\frac{\gamma-1}{\gamma}} - 1\right] \cdot W_{\mathrm{cp}} \tag{2}$$

where C_{air} is the specific heat capacity of air, J/(kg · K); $T_{\mathrm{cp,in}}$ is the air inlet temperature of the compressor; $P_{\mathrm{cp,in}}$ is the air inlet pressure of the compressor, Pa; $P_{\mathrm{cp,out}}$ is the air outlet pressure of the compressor, Pa; γ is the ratio of specific heat capacity at atmospheric pressure; W_{cp} is the compressor outlet air flow rate, kg/s; η_{cp} is the working efficiency of the compressor.

2.2.2 | Supply Pipe Model

The air supply pipe is the medium that connects the components of the air supply system and drives the reaction gases into the reactor. The supply pipe outlet flow rate $W_{\mathrm{sm,out}}$ can be expressed as:

$$W_{\mathrm{sm,out}} = k_{\mathrm{sm,out}} \cdot (P_{\mathrm{sm}} - P_{\mathrm{ca}}) \tag{3}$$

where $k_{\mathrm{sm,out}}$ is the resistance to flow in the supply pipe, P_{sm} is the inlet pressure to the supply pipe, Pa, and P_{ca} is the cathode pressure, Pa.

$$\frac{\mathrm{d}P_{\mathrm{sm}}}{\mathrm{d}t} = \frac{\gamma \cdot R_{\mathrm{air}}}{V_{\mathrm{sm}}}(W_{\mathrm{cp}} \cdot T_{\mathrm{cp}} - W_{\mathrm{sm,out}} \cdot T_{\mathrm{sm}}) \tag{4}$$

where R_{air} is the air gas constant, J/(kg · K); V_{sm} is the supply pipe volume, m^3; and T_{sm} is the fluid temperature in the supply pipe, K.

2.2.3 | Intercooler and Humidifier Model

Since the air leaving the compressor is very hot, it must be cooled to the operating temperature of the stack to prevent damage to the proton exchange membrane in the fuel cell stack. It is assumed that the fuel cell operates at a constant temperature of 80°C and that there is no pressure drop as the gas passes through the cooler. The humidity of the gas exiting the cooler is calculated as follows:

$$\phi_{\mathrm{cl}} = \frac{P_{\mathrm{v,cl}}}{P_{sat}(T_{\mathrm{cl}})} = \frac{P_{\mathrm{cl}} \cdot P_{\mathrm{v},atm}}{P_{atm} \cdot P_{sat}(T_{\mathrm{cl}})} = \frac{P_{\mathrm{cl}} \cdot \phi_{atm} \cdot P_{sat}(T_{atm})}{P_{atm} \cdot P_{sat}(T_{\mathrm{cl}})} \tag{5}$$

where ϕ_{atm} is the relative humidity of the air; $P_{sat}(T_{\mathrm{cl}})$ is the vapour saturation pressure, Pa; and P_{cl} is the air pressure in the intercooler, Pa.

Water is injected into the air stream and passes through the humidifier to humidify the output air stream from the intercooler before it reaches the electric stack. The change in air humidity is calculated using a static humidifier model. It is assumed that the air stream's temperature is constant, $T_{hm} = T_{cl}$, and that the water used for humidification is vapour. The water vapour saturation pressure is derived from the temperature of the water stream, and subsequently, the water vapour pressure, as denoted by

$$P_{\mathrm{v,hm}} = \varphi_{\mathrm{hm}} \cdot P_{sat,T} \tag{6}$$

The incremental water vapour flow in the air after humidification is expressed as:

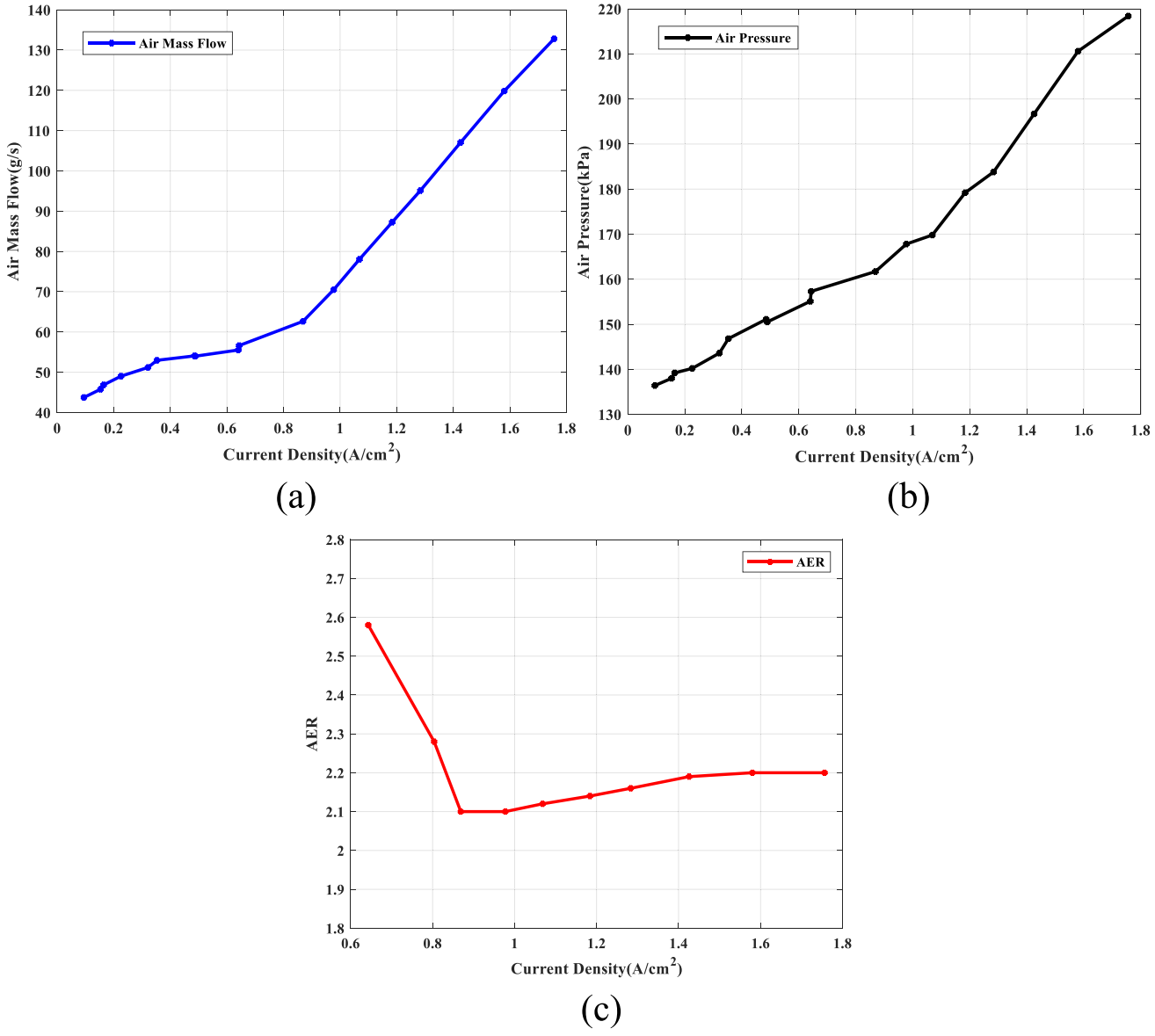

FIGURE 5 | Plot of current density against air flow, air pressure, and AER at standard operating conditions. (a) Current density versus air flow. (b) Current density versus air pressure. (c) Current density versus AER.

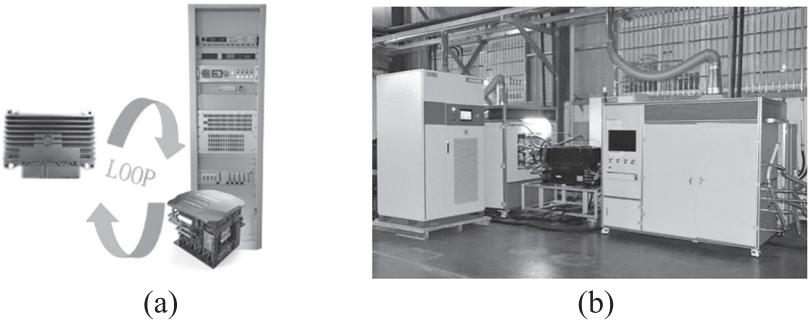

FIGURE 6 | Fuel cell engine control closed loop and test environment. (a) Schematic diagram of closed-loop automatic control. (b) Engine testing environment.

TABLE 3 | Test equipment related parameters.

Items	Range	Precision	Items	Range	Precision
Voltage	0–500 V	$\leq \pm 0.5\%$FS	Temperature	−40–140°C	$\leq \pm 1\%$
Current	0–1000 A	$\leq \pm 0.5\%$FS	Air pressure	0–3 bar	$\leq \pm 2\%$
Air flow	0–800 kg/h	$\leq \pm 2\%$	Relative humidity	0–100%RH	$\leq \pm 0.8\%$

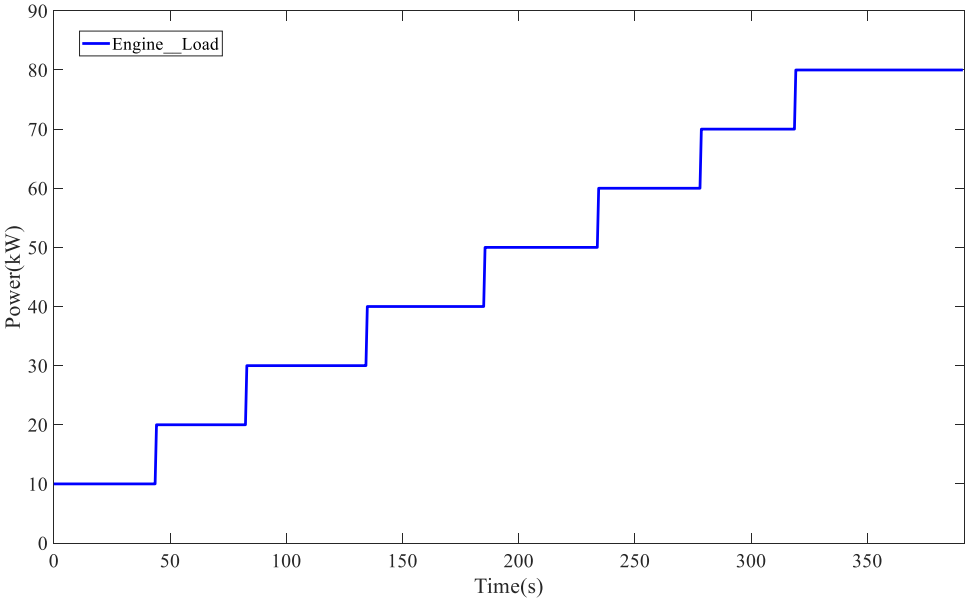

FIGURE 7 | Engine Load in the loading stage.

$$W_{\mathrm{v,in}} = W_{\mathrm{v,hm}} - W_{\mathrm{v,cl}} = \frac{M_{\mathrm{v}}}{M_{\mathrm{a,cl}}} \cdot \frac{P_{\mathrm{v,hm}}}{P_{\mathrm{a,cl}}} \cdot W_{\mathrm{a,cl}} - W_{\mathrm{v,cl}} \quad (7)$$

where $W_{\mathrm{v,hm}}$ and $W_{\mathrm{a,cl}}$ are the water vapour mass flow rate after humidification and the water vapour mass flow rate before humidification, respectively, kg/s; Mv and Ma,cl are the molar mass of water vapour and the molar mass of dry air, respectively, kg/mol; $P_{\mathrm{v,hm}}$ and $P_{\mathrm{a,cl}}$ are the partial pressure of water vapour and the partial pressure of dry air inside the humidifier, respectively, Pa.

$$P_{\mathrm{a,cl}} = P_{\mathrm{cl}} - P_{\mathrm{v,cl}} \quad (8)$$

The total gas pressure in the humidifier pipework is represented by

$$P_{\mathrm{hm}} = P_{\mathrm{a,cl}} + P_{\mathrm{v,hm}} \quad (9)$$

The humidity ratio in a humidifier could be expressed as

$$\omega_{\mathrm{cl}} = \frac{M_{\mathrm{v}}}{M_{\mathrm{a,cl}}} \cdot \frac{P_{\mathrm{v,hm}}}{P_{\mathrm{a,cl}}} \quad (10)$$

The relative humidity of the outlet gas is denoted by

$$P_{\mathrm{v,hm}} = \omega_{\mathrm{cl}} \cdot \frac{M_{\mathrm{a,cl}}}{M_{\mathrm{v}}} \cdot P_{\mathrm{a,cl}} \quad (11)$$

$$\phi_{\mathrm{rh}} = \frac{P_{\mathrm{v,hm}}}{P_{\mathrm{sat,T}}} \quad (12)$$

The outlet flow rate of the humidifier is the inlet flow rate to the cathode, which could be represented as

$$W_{\mathrm{hm}} = W_{\mathrm{a,cl}} + W_{\mathrm{v,hm}} = W_{\mathrm{a,cl}} + W_{\mathrm{v,cl}} + W_{\mathrm{v,in}} \quad (13)$$

2.2.4 | Return Pipeline Model

The primary function of the return pipe is to discharge residual gas from the reactor after participating in the chemical reaction. It is assumed that the temperature within the return pipe is the same as that of the gas exiting the cathode. The mass of gas in the return pipe can be expressed as [41]

$$\frac{dm_{\mathrm{rm}}}{dt} = W_{\mathrm{rm,in}} - W_{\mathrm{rm,out}} \quad (14)$$

where m_{rm} is the mass of material in the supply pipe; $W_{\mathrm{rm,in}}$ and $W_{\mathrm{rm,out}}$ are the gas flow rate at the inlet and outlet of the return pipe, respectively, kg/s. The pressure in the return pipe is

$$\frac{dP_{\mathrm{rm}}}{dt} = \frac{T_{\mathrm{rm}} \cdot R_{\mathrm{air}}}{V_{\mathrm{rm}}} \cdot (W_{\mathrm{ca,out}} - W_{\mathrm{rm,out}}) \quad (15)$$

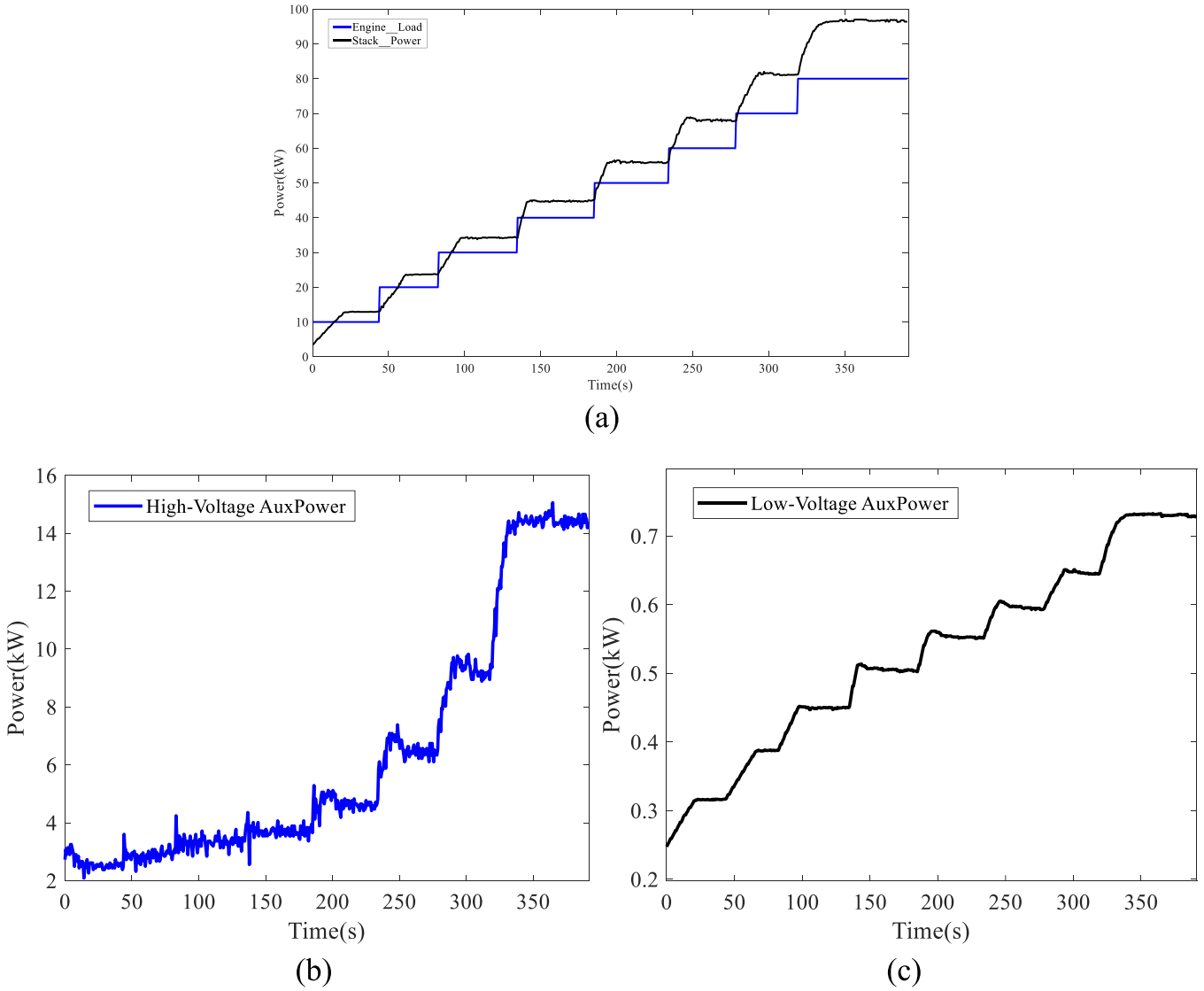

FIGURE 8 | Engine load, stack output power, and auxiliary power in the loading stage. (a) Comparison of the stack output power with the engine load in the loading stage. (b) High-voltage auxiliary power. (c) Low-voltage auxiliary power.

where P_{rm} is the pressure in the return pipe, Pa; T_{rm} is the temperature of the gas in the return pipe, K; V_{rm} is the volume of the return pipe, m^3; $W_{\mathrm{rm,out}}$ is the gas flow rate at the outlet of the return pipe, kg/s. The gas flow rate at the outlet of the return pipe can be indicated as

$$W_{\mathrm{rm,out}} = \begin{cases} \dfrac{rm_0 \cdot A_T \cdot P_{\mathrm{rm}}}{\sqrt{RT_{\mathrm{rm}}}} \left(\dfrac{P_{atm}}{P_{\mathrm{rm}}}\right)^{\frac{1}{\gamma}} \sqrt{\dfrac{2\gamma}{\gamma-1}\left[1-\left(\dfrac{P_{\mathrm{atm}}}{P_{\mathrm{rm}}}\right)^{\frac{\gamma-1}{\gamma}}\right]} & \dfrac{P_{\mathrm{atm}}}{P_{\mathrm{rm}}} > \left(\dfrac{2}{\gamma+1}\right)^{\frac{\gamma}{\gamma-1}} \\ \dfrac{rm_0 \cdot A_T \cdot P_{\mathrm{rm}}}{\sqrt{RT_{\mathrm{rm}}}} \gamma^{\frac{1}{2}} \cdot \left(\dfrac{2}{\gamma+1}\right)^{\frac{\gamma+1}{2(\gamma-1)}} & \dfrac{P_{\mathrm{atm}}}{P_{\mathrm{rm}}} \leq \left(\dfrac{2}{\gamma+1}\right)^{\frac{\gamma}{\gamma-1}} \end{cases} \tag{16}$$

where rm_0 is the nozzle flow coefficient; A_T is the cross-sectional area of the return pipe, m^2; R is the universal gas constant, J/(kg · K); γ is the ratio of the specific heat capacity of the gas Cp/Cv. In the case of air $\gamma = 1.4$, the critical pressure ratio equals 0.528. A_T is calculated as follows

$$A_T = \pi \cdot r^2 \cdot \theta \tag{17}$$

where r is the backpressure valve opening radius, m; θ is the backpressure valve opening angle.

An air supply system simulation model was developed using the MATLAB/Simulink platform. Polynomial fitting and parameter identification were conducted to enhance accuracy based on data obtained during actual fuel cell engine operation. This model serves as the foundation for the subsequent verification of the PID controller's reliability.

2.3 | Air Mass Flow and Pressure Control Objectives

Air compressor speed and the opening degree of the back pressure valve were the control variables for the air supply system in this study. To guarantee that the fuel cell system would provide the appropriate amount of electricity, the air flow and pressure were precisely regulated to reach the specified parameters. The air excess ratio (AER) $\lambda(t)$ was used to calculate the air mass flow supply, shown in Equation (18). The air flow rate required for the reaction $W_{air,rec}$ was calculated by Equation (19).

$$\lambda(t) = \frac{w_{air,in}(t)}{w_{air,rec}(t)} \tag{18}$$

$$W_{air,rec} = \frac{V_{m,air} N I_{st}}{4F \times 0.21} \tag{19}$$

where $w_{air,in}(t)$ denotes the actual gas supply, g/s; $w_{air,rec}(t)$ denotes the amount of air required for the reaction, g/s; $V_{m,air}$ denotes the molar volume of gas, L/mol; N is the number of individual cells; F stands for the Faraday constant; I_{st} stands for the electric stack's current, A.

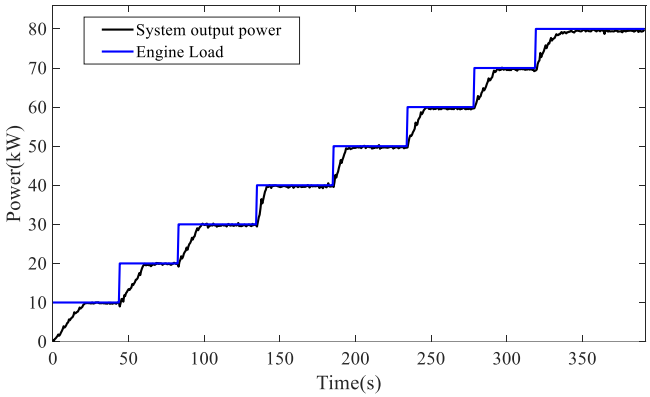

FIGURE 9 | Comparison of system output power with engine load in the loading stage.

2.4 | Principles of Control Algorithms and Control Logic

Most existing controllers focus on regulating the air mass flow rate by controlling the OER while neglecting to regulate

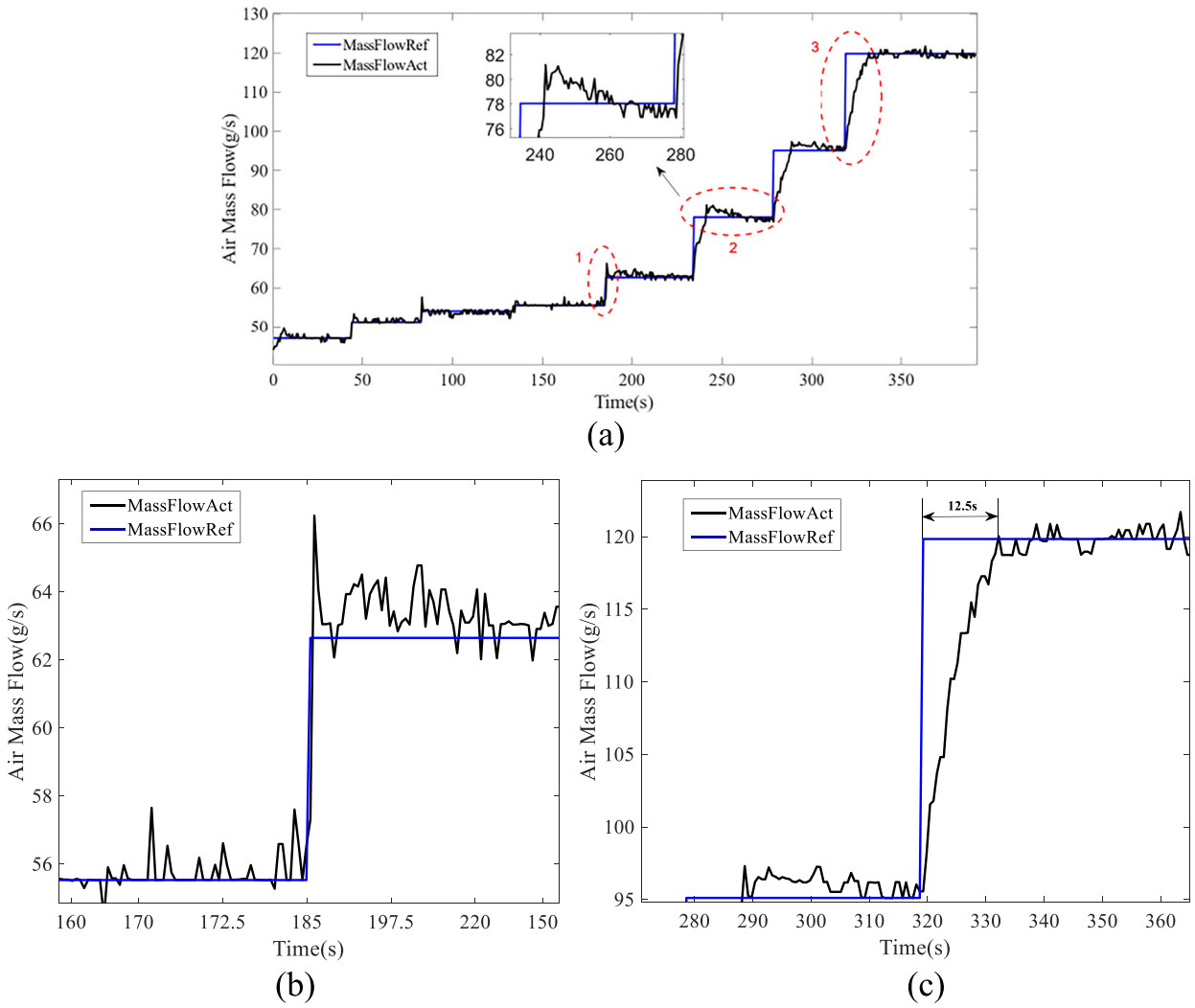

FIGURE 10 | Comparison and enlarged air flow view following the loading stage curve. (a) Comparison of actual air flow rate with reference air flow rate in the loading stage. (b) Enlarged view of red ellipse 1 in Figure 8a. (c) Enlarged view of red ellipse 3 in Figure 8a.

air pressure. Since air flow and pressure are strongly coupled and nonlinear, their interdependence significantly impacts the performance of high-power fuel cell systems. Therefore, accurate air mass flow and pressure control are essential for optimal fuel cell performance. The traditional PID approach is commonly used due to its simplicity and robustness [42]. The mathematical expression of the PID approach is:

$$y(t) = k_p e(t) + k_i \int e(t)dt + k_d \frac{de(t)}{dt} \tag{20}$$

where e represents the feedback deviation.

This manuscript introduces an enhanced feed-forward dual-loop segmented PID controller for the air supply system, combining feed-forward and traditional PID control. Figure 3. illustrates the schematic diagram of the feed-forward PID control logic. The proposed scheme features two main modules: one for feed-forward control and another for feedback bias-based parameter segmentation and tuning. Additionally, it includes PID control and feedback modules for comprehensive monitoring.

The core components of the flow control system involve calculating flow deviation and its rate of change, setting segmented PID parameters, referencing a feed-forward parameter lookup table, and performing PID calculations. Integral anti-saturation measures are incorporated into the PID calculation module to prevent excessive accumulation. These measures are triggered when the integral output term or the calculated compressor rotation speed exceeds predefined limits.

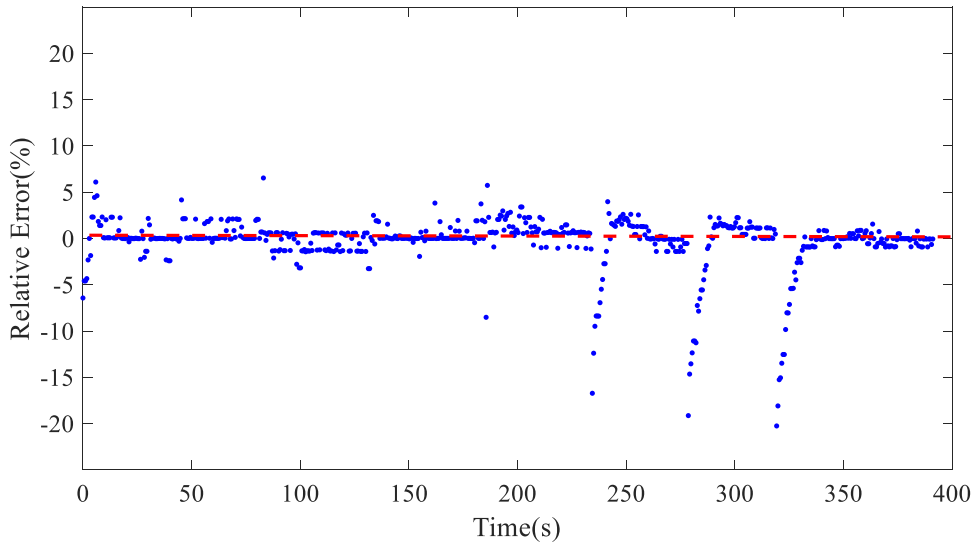

FIGURE 11 | Air flow relative deviation distribution.

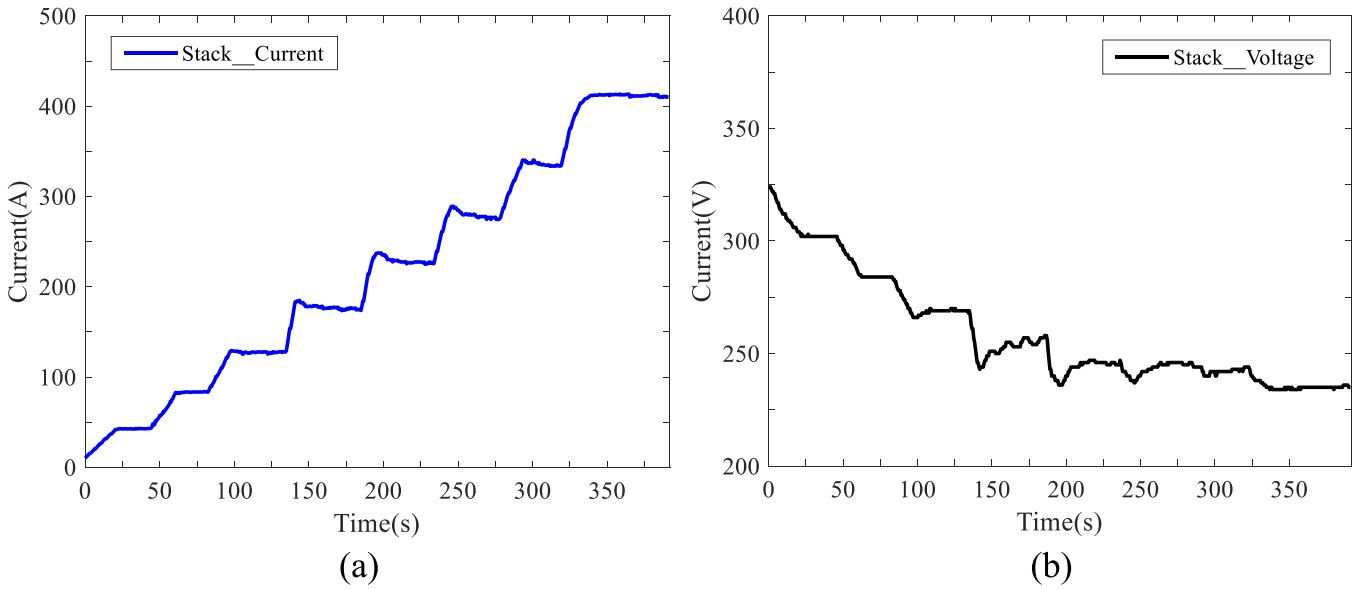

FIGURE 12 | Curves of the stack voltage and current in the loading stage. (a) Current curve. (b) Voltage curve.

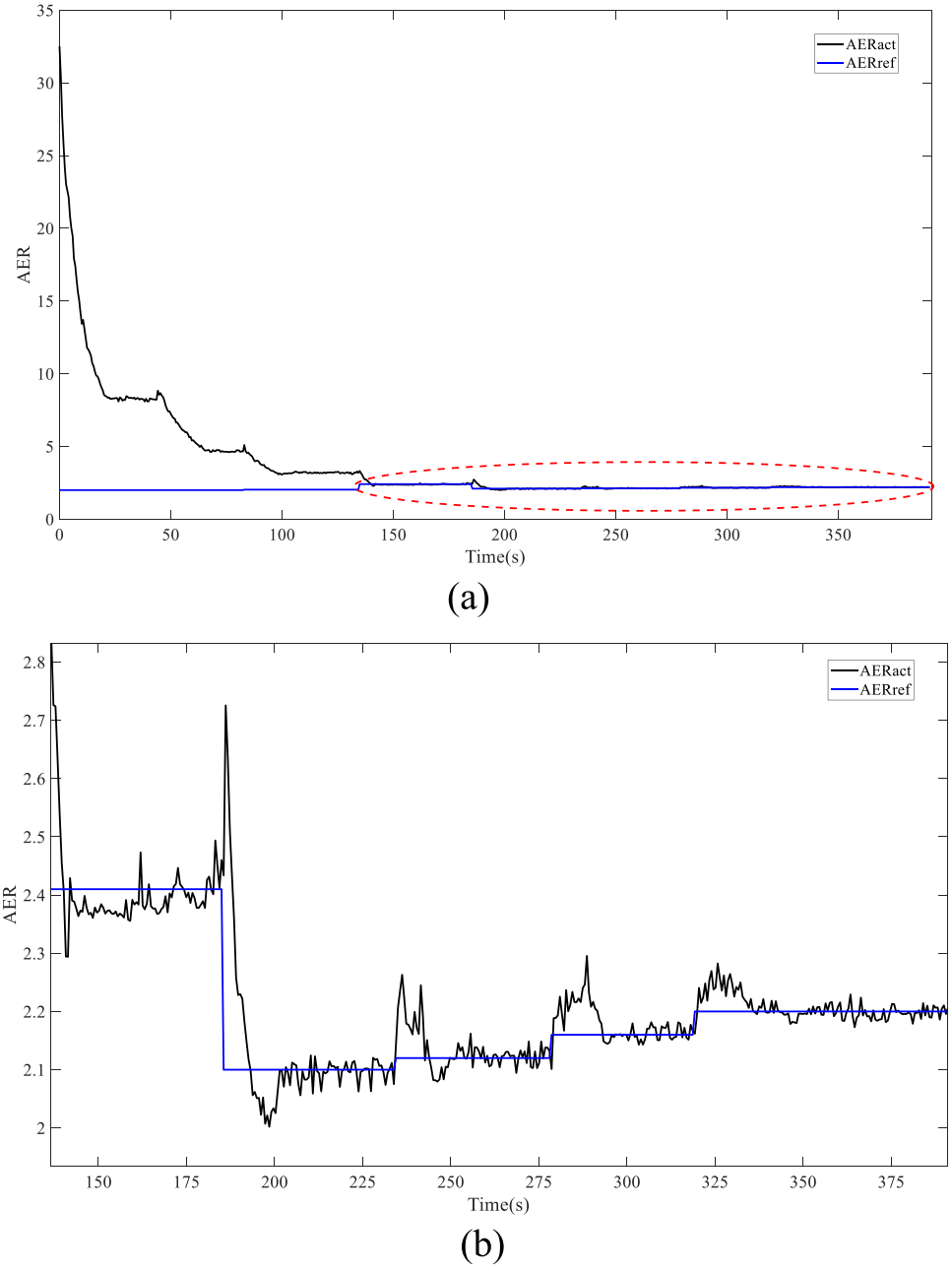

FIGURE 13 | Comparison and enlarged view of the AER. (a) Actual AER versus reference AER in the loading stage. (b) Enlarged view of the red oval portion of Figure 11a.

Additionally, the magnitude of the increase or decrease and the extreme values of the compressor rotation speed were constrained. The core of the pressure control involved closed-loop regulation of the air inlet pressure using a PID algorithm with feedforward compensation. This control process included calculating the air inlet pressure deviation and its rate of change, setting segmented PID parameters, referencing a feedforward parameter lookup table, and performing PID calculations while maintaining the air inlet reference pressure within the surge limit of the air compressor.

A dead zone was established for the air inlet pressure deviation to prevent oscillations in the backpressure valve opening and air flow rate. When the deviation was within this dead zone's upper and lower limits (indicating a minor difference from the reference pressure), the back pressure valve opening from the previous moment was retained. If the air inlet pressure deviation exceeded the dead zone, the backpressure valve adjusted its opening based on the PID calculation results. The amplitude of changes in the backpressure valve position and its extreme values were limited to avoid oscillations in air inlet pressure caused by rapid fluctuations in the backpressure valve position.

At the same time, when the backpressure valve control was enabled but did not need to regulate the air inlet pressure, the backpressure valve was maintained at a fixed opening position. Upon receiving a demand request for power (or current), the controller first determined whether the system

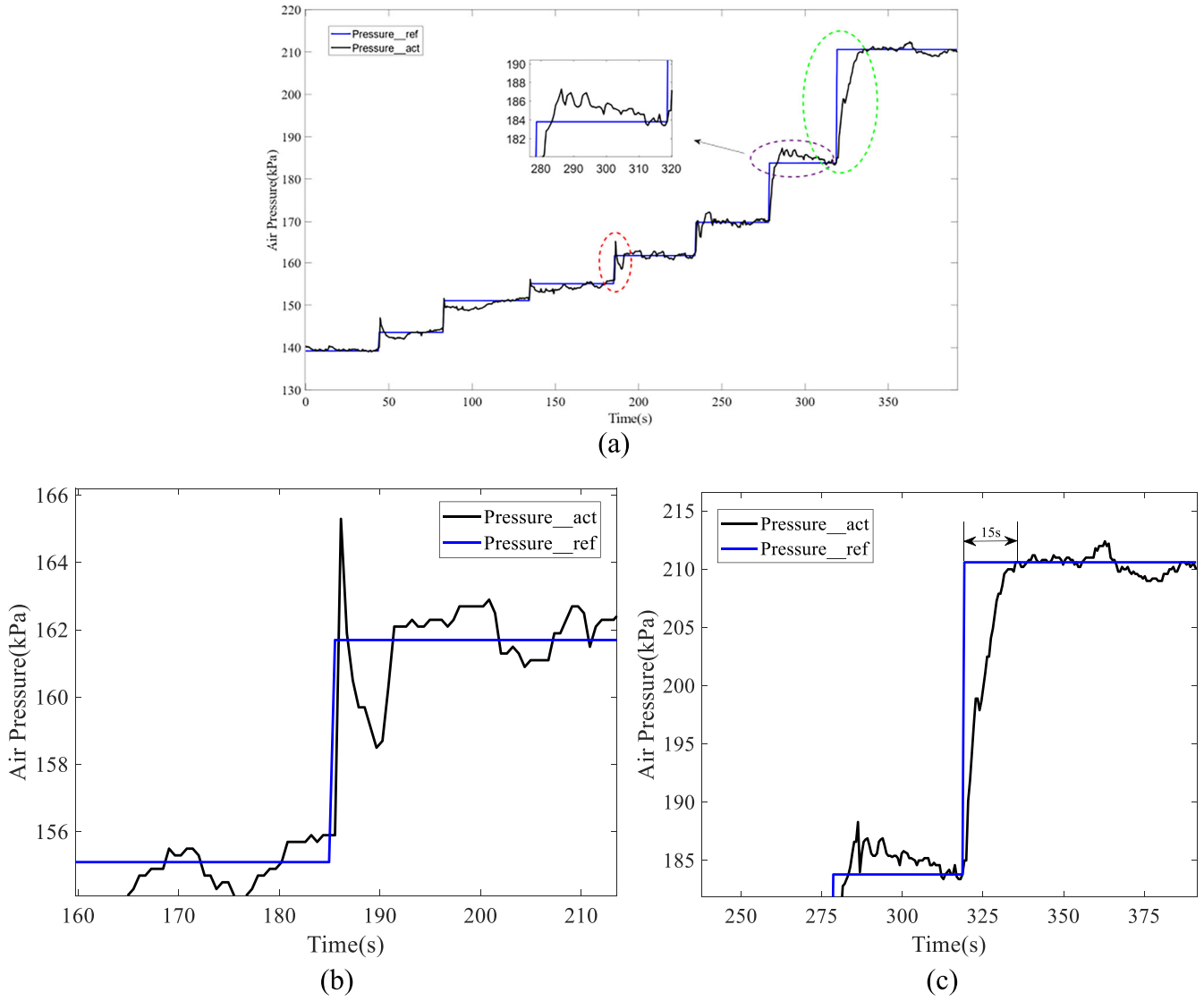

FIGURE 14 | Response curve and enlarged view of air pressure. (a) Response curve of cathode inlet air pressure in the loading stage. (b) Enlarged view of the red oval portion. (c) Enlarged view of the green oval portion.

was in a fault-limited power state. If so, it outputted fault coefficients under different faults to reduce the requested current. Subsequently, according to the feedback current of the air compressor, heater, and cooling water pump, the demand value of the system was calculated to get the reference value of the air flow. Then, the PID controller received the computed deviation from the system's reference and actual values to get the calculated speed value. Finally, according to the actual cathode air inlet pressure and air flow reference value to the air compressor speed feed-forward value, the two were added to get the air compressor speed signal and sent to realise speed control. Similarly, according to the air flow reference value to get the cathode inlet air pressure reference value and BPV feed-forward opening value, the feed-forward opening value and the PID calculation value were added to get the output valve. These two actuators reacted to the control signal they received to satisfy the PEMFC system's air pressure and mass flow criteria.

In addition, the control strategy mitigates ohmic losses during startup and shutdown by combining a feed-forward PID with transient parameter optimisation. During transients, the feed-forward module preadjusts the air flow according to the operating phase to reduce membrane dehydration and contact resistance peaks. And the dual PID loops are dynamically adjusted via segmented look-up tables to maintain optimal hydration. Backpressure valve oscillations that disrupt reactant distribution are reduced by limiting compressor speed overshoot and setting pressure dead zones. Reduce ohmic resistance fluctuations and lower ohmic losses by combining predictive feed-forward and feedback corrections to stabilise membrane ionic conductivity and component contact state. The parameters of the PID controller designed in this manuscript are detailed in Table 2. Parameters were tuned via iterative simulations using the MATLAB/Simulink model, prioritising transient response time (< 15 s) and overshoot of air pressure ($<5\%$).

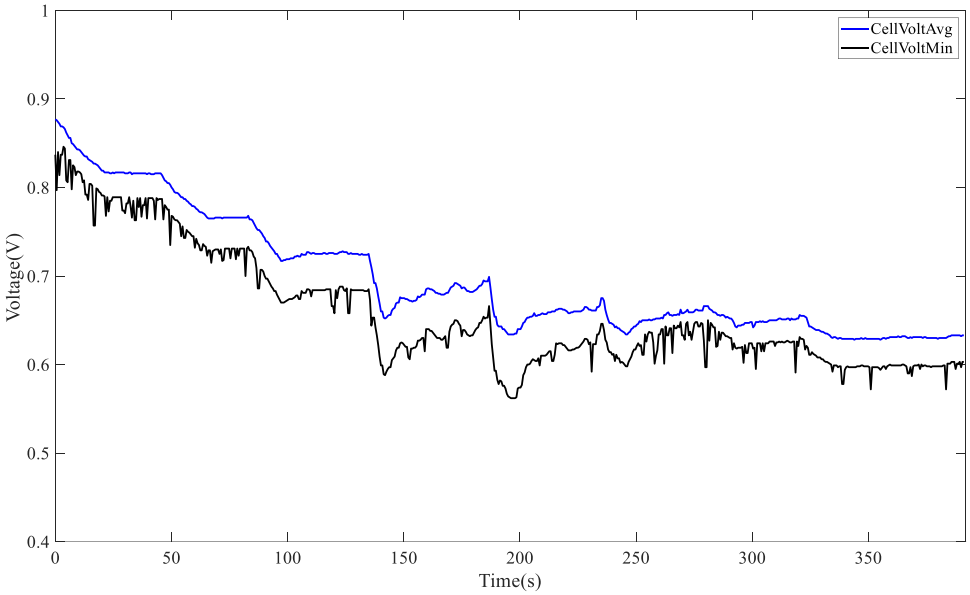

FIGURE 15 | Minimum single-cell voltage versus average single-cell voltage.

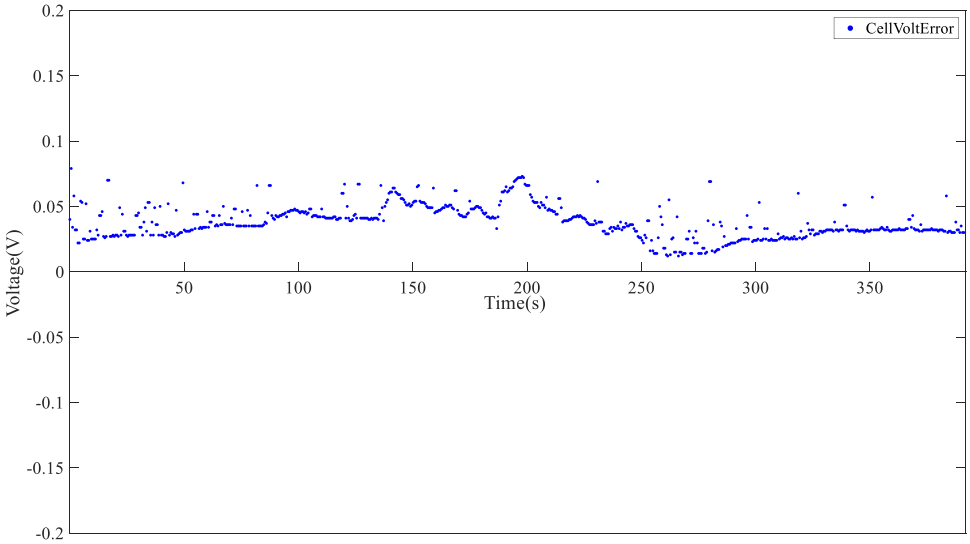

FIGURE 16 | The disparity of the average and lowest voltages of single-cell.

3 | Experimental Setup

3.1 | Selection of Reference Operating Point

The stack's performance can be judged according to the average voltage of the single cell under different operating conditions. The larger the average single-cell voltage was, the higher the power generation efficiency of the stack would be. Therefore, the working condition with the highest average single-cell voltage was set as the standard operating condition, and the engine's performance parameters under this working condition were the reference values. In addition, the air compressor was the high-pressure auxiliary component, and its power was much larger than the rest of the auxiliary components. The air compressor's ideal operating point had to be determined to increase power production efficiency. In addition, the minimum speed of the air compressor was set to maintain the minimum air flow rate and perform surge protection to guarantee the stability of the air compressor's operation. The optimal AER indicated the air compressor's current optimal parasitic power.

Based on these criteria, sensitivity tests were performed on the fuel cell stack before assembling the 86 kW-grade fuel cell engines. The tests compared the physical parameters of the cathode and anode reaction media, as well as the voltage and current outputs of the stack under various operating conditions. Subsequently, data were collected for the single-cell average voltage, stack current, air flow rate, air pressure, and AER at the optimal operating point for each condition. Additionally, polarisation curves showing the relationship between single-cell average voltage and current density were generated, as illustrated in Figure 4. Concurrently, current density was used as a reference to determine the corresponding air flow, air pressure, and AER, as depicted in Figure 5.

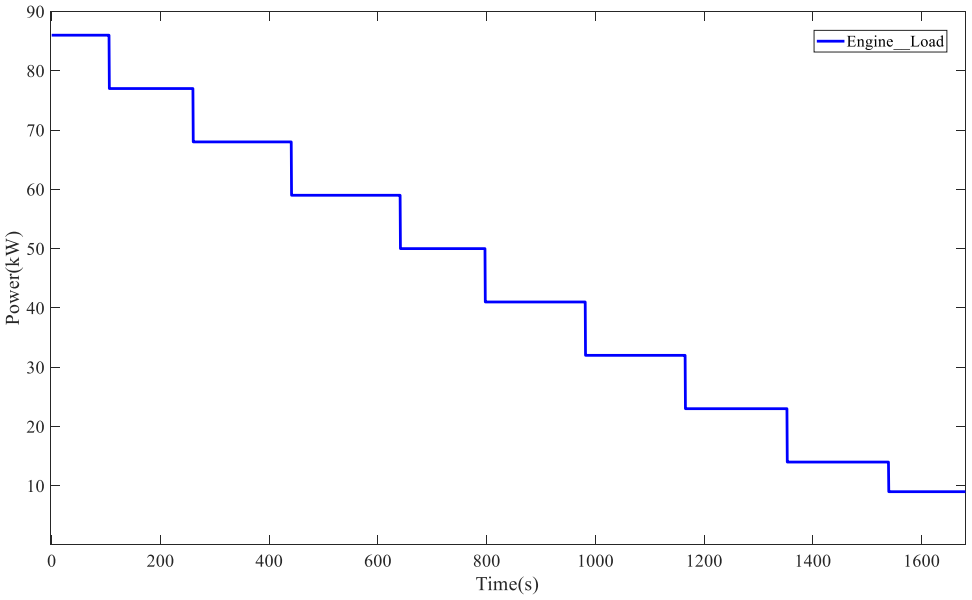

FIGURE 17 | Engine load in de-loading stage.

3.2 | Test Bench Structure and Experimental Procedure

As depicted in Figure 6a, the hardware setup for the control closed-loop experiment includes a fuel cell system controller, a fuel cell engine, and a control cabinet. The testing was conducted in the engine test environment illustrated in Figure 6b. The test bench primarily consisted of a control and monitoring platform encompassing water, gas, electrical circuits, and corresponding temperature, pressure, flow sensors, and valves.

The water circuit measured and controlled the temperature, pressure, and flow of the primary and auxiliary components. In contrast, the air circuit managed measurements and control for air and hydrogen temperature, pressure, and flow. The electrical circuits included a load bank to absorb the electrical power generated by the engine, a low-voltage distribution box to supply power to various engine actuators, and a system for transmitting and receiving measurement and control signals through the test bench's host computer.

Table 3 Summarises the relevant settings for the test equipment. The control model was initially developed in MATLAB/Simulink. The Simulink Coder toolbox was then employed to generate code for the model. Subsequently, an embedded software development tool was used to compile the automatically generated C code and deploy it to the controller.

Before initiating the tests, gas-tightness and insulation tests were conducted. The pipeline was purged with nitrogen before and after the test to remove residual water or hydrogen, thereby preventing flooding or low-temperature icing. As hydrogen follows a sealed gas path, impurities, cathode gas permeation, and water vapour accumulation during operation can gradually reduce the anode hydrogen concentration and affect the mass transfer. Therefore, hydrogen was periodically discharged to mitigate these issues.

At the start of the experiment, the system was powered on and underwent a start-up process as dictated by the state machine commands. Initially, the actuator was set to its starting position and gradually increased speed according to the predefined sequence.

4 | Experimental Results and Discussion

This section applied the proposed control technique to a real fuel cell engine using a test bench to assess its effectiveness. The experimental process was divided into three main stages: the loading stage, the de-loading stage, and the stage involving a wide range of sudden load changes.

4.1 | Loading Stage

Figure 7 illustrates the load variation during the loading stage, while Figure 8a shows the comparison between the engine load and the stack's actual power output. As depicted in Figure 8a, the fuel cell system stabilises as the load varies, with the stack's actual output power exceeding the load. This discrepancy occurs because the auxiliary components consume a portion of the stack's output power, and their power consumption fluctuates with operating conditions, as shown in Figure 8b,c. Consequently, the stack must generate power exceeding the engine load to compensate for the power consumption of these auxiliary parts. The output power of the fuel cell system, referred to as the system's output power, is calculated by subtracting the power consumed by the auxiliary components from the stack's actual output power. The low-voltage auxiliary components consumed less than 1 kW of power during the loading stage, as indicated in Figure 8c. Conversely, the air compressor, a high-voltage auxiliary component, consumed ~20% of the stack's output power (see Figure 8b). This substantial power consumption by the air compressor significantly influences the system's overall output performance. Therefore, the performance of the fuel cell system is heavily dependent on the operation of the air compressor.

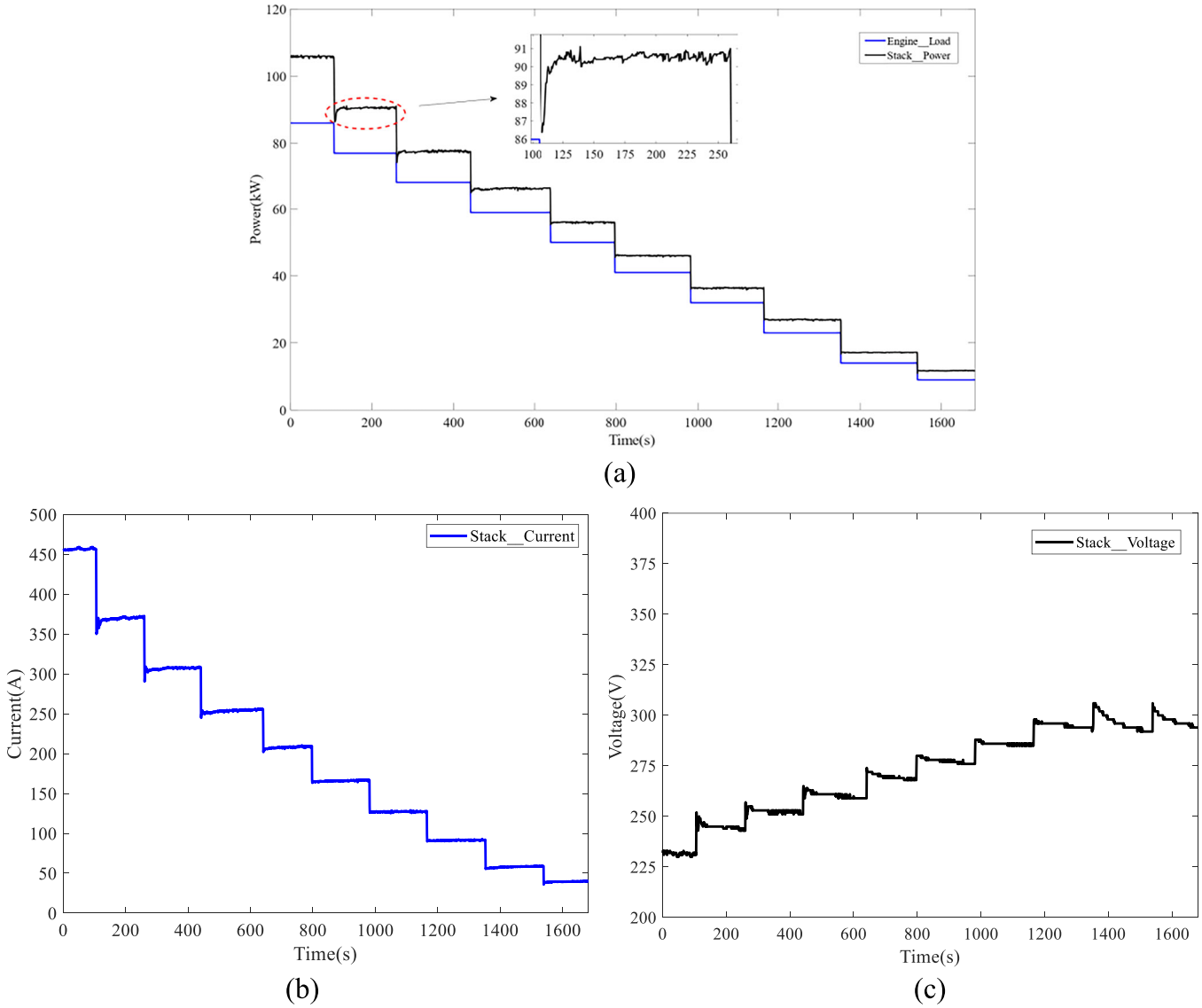

FIGURE 18 | Engine load, stack output power, current, and voltage in the de-loading stage. (a) Comparison of output power of the stack with engine load in the de-loading stage. (b) Current output curve. (c) Voltage output curve.

Figure 9 compares the system output power with the load, illustrating that as the load increases, the system output power gradually rises until it stabilises, smoothly following the load step change. Due to the limited rate of current rise during loading, the time required for the system output power to reach the desired level increases with higher loads. The maximum regulation time observed during the loading stage was 20 s, with no noticeable overshoot in power.

Figure 10a illustrates the contrast between the air flow actual and reference values under loading conditions. When the load was low (10-40 kW), the actual air flow rate followed the reference air flow rate better, but there was a slight fluctuation around the reference air flow rate. The deviation between the actual and reference air flow increased when the load was high (50-80 kW). Figure 10b,c show a zoomed-in view of the air flow rate following the curve in the loading stage, whereas Figure 10b,c are zoomed-in views of parts 1 and 3 of the red ellipse, respectively. The range of air mass flow rate fluctuation was the largest when the system operated stably at the load of 60 kW when the average deviation value was 1.6 g/s. The actual air flow rate had different sizes of overshooting and regulation time at different loading moments, where the maximum overshooting was less than 4 g/s (as shown in Figure 10b), and the longest transient time was 12.5 s (as shown in Figure 10c).

The transmission mechanism of internal mass and the reactant supply rule were connected to the regulation time. The system loading process first increased the work material, and the chemical reaction subsequently generated the current, so the current loading lagged. When the air mass flow rate increased rapidly, the humidity change was relatively slow, which affected the reaction efficiency, and the system would limit the current loading speed in the low voltage of a single cell. Therefore, the current and air mass flow rate at the later period of the loading stage is reduced.

The reason for limiting the current loading speed was that when the system was running at high power, the current rising too quickly would cause massive heat generation in the system, and the high temperature led to a decrease in engine efficiency or

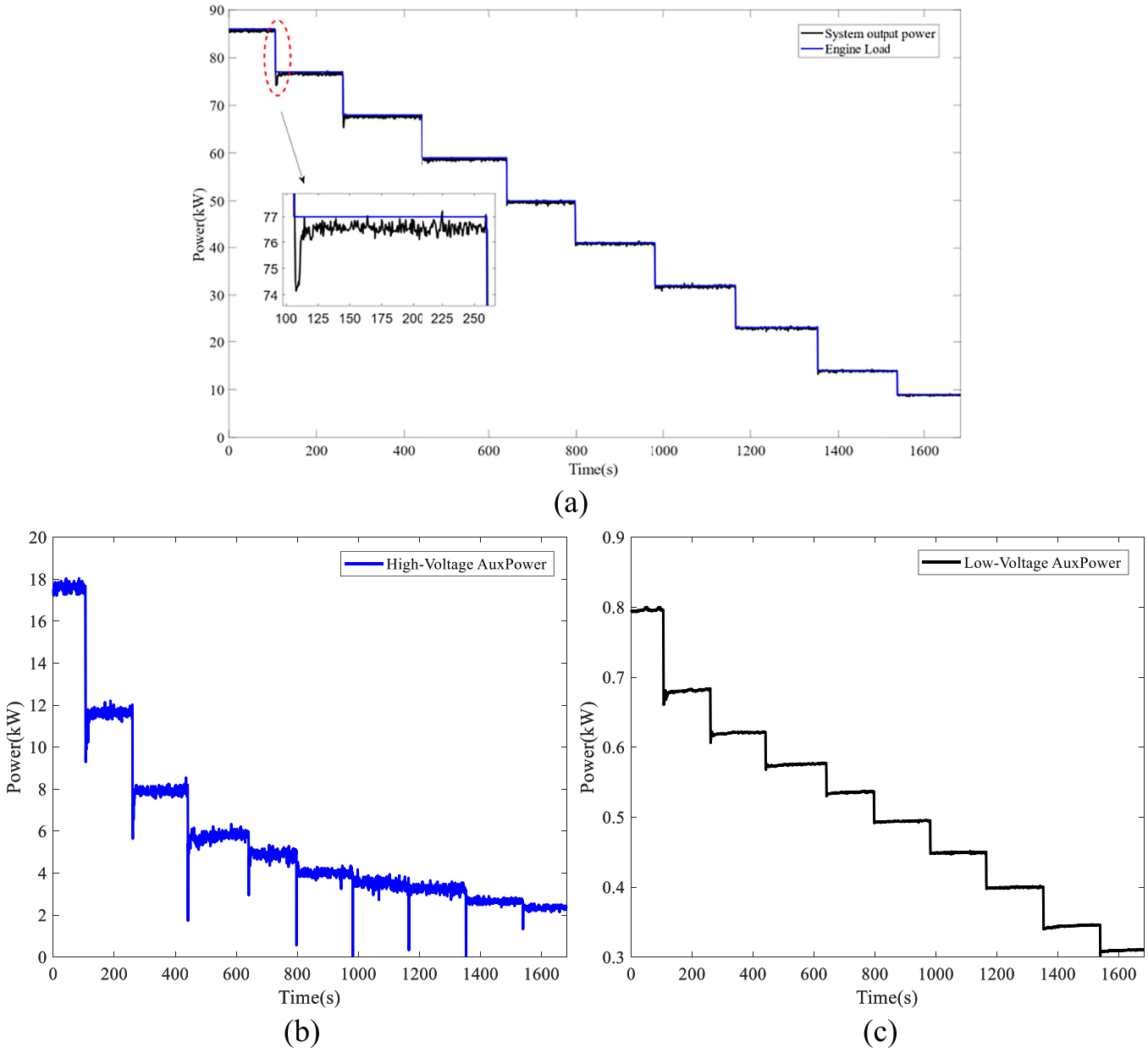

FIGURE 19 | Engine load, system output power, and auxiliary power in the de-loading stage. (a) System output power versus engine load in the de-loading stage. (b) High-voltage auxiliary power. (c) Low-voltage auxiliary power.

even damage. Figure 11 shows the relative deviation, and the calculation formula is shown in Equation (21). From Figure 11, it is evident that there is a slight relative variance in the air mass flow rate; the maximum relative deviation value is 20%, and it arises at the moment of instantaneous change of demanded power.

$$\delta = \frac{y_i - r_i}{r_i} \times 100\% \tag{21}$$

where δ denotes the relative deviation; y_i denotes the air mass flow rate in actual conditions, g/s; and r_i denotes the air mass flow rate reference value, g/s.

The stack's output curves for voltage and current during the loading stage are shown in Figure 12. In Figure 12a, the stack current rises steadily with the increase of the load, and the current fluctuates only in a small range after the fuel cell is stabilised under different load. It is evident from Figure 12b that the overall stack voltage decreases, with a small undershoot during the transient process, followed by stabilisation quickly. Under larger loads (50–80 kW), the voltage of the stack was stable, with minor changes in the steady-state and transient process.

The contrast of the loading stage AER in different conditions is displayed in Figure 13a. When the load was small (10–40 kW), the target current was small, and the system had a minimum air flow limit. The theoretically required air flow was much lower than the minimum air flow limit, resulting in a significant difference between the actual AER and the reference value (shown in Figure 13a). The reference air

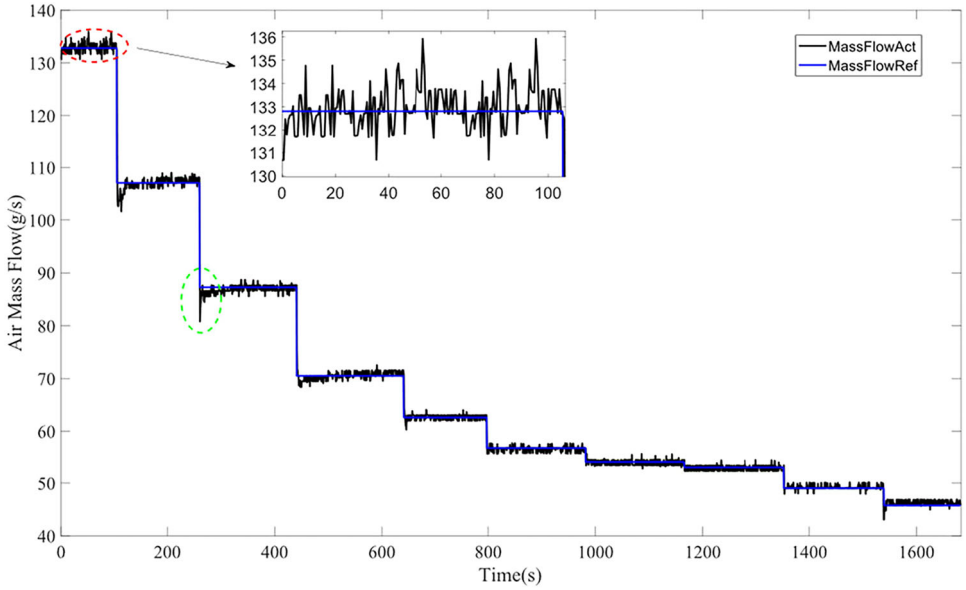

FIGURE 20 | Comparison of actual air flow and reference air flow in the de-loading stage.

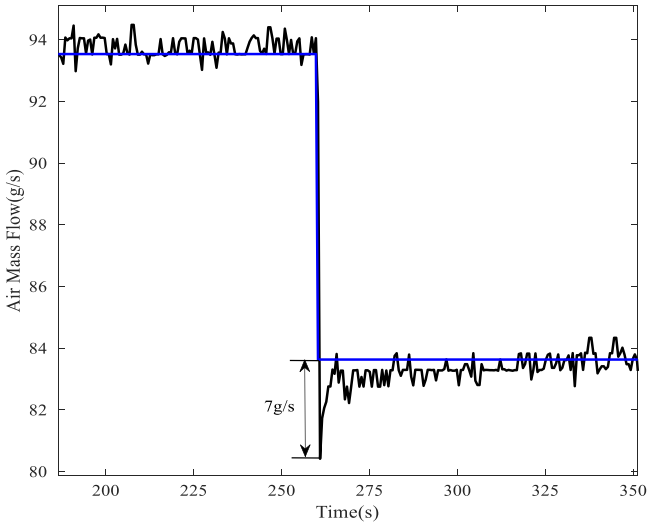

FIGURE 21 | Enlarged view of the green oval portion of Figure 19.

flow rate exceeded the minimum flow limit as the load increased. Figure 13b shows the enlarged red ellipse portion of Figure 13a.

The actual AER at higher power (50–80 kW) was able to follow the reference AER well, with an average deviation range of ±0.04. During transient and steady-state activities, the difference between the actual and reference AER values steadily reduced as the load rose. Because of the strong coupling effects, it is necessary to control the cathode inlet air pressure while controlling the air flow to maintain the normal cathode and anode pressure difference to avoid the membrane being damaged and, at the same time, to keep the system in the optimal working interval. The cathode inlet air pressure response curve during the loading stage is displayed in Figure 14a. The overall fluctuation range of the air pressure during the loading process was small, and the maximum air pressure overshoot was 4 kPa (as shown in Figure 14b). When the demand pressure changed abruptly, the longest adjustment time for the actual pressure to reach the demand pressure was 15 s (as shown in Figure 14c), and the air pressure deviation was the largest under the 70 kW load, with an average deviation range of ±1.82 kPa.

The fuel cell stack consisted of 370 single cells connected in series, and due to the large number of single cells, the impact of each cell on the air supply system controller would be reflected in the output. Therefore, the single-cell voltage variation reflected the effect of the air control strategy. Figure 15 shows the variation of the average and lowest voltages of single cells under different loads. As the amount of power required increased during the loading stage, the single-cell voltage gradually decreased. The variation between the loading stage average and the lowest voltage of a single cell is seen in Figure 16. Overall, the difference between the two was minimal, mostly under 0.05 V, indicating that the stack's single-cell voltage was relatively consistent.

4.2 | De-Loading Stage

As seen in Section 4.1, when the system is loading, the air supply system control strategy ensures the holding effect under various demands during transient and steady state. Therefore, it is necessary to analyse the effectiveness of this controller further in controlling the mass flow rate and pressure in the de-loading stage.

Figure 17 shows the load curve of the engine in the de-loading stage. Figure 18a illustrates the stack's power output versus engine load in the de-loading stage. The intervals where the maximum power undershoots and steady-state fluctuations occurred in the de-loading stage are shown in the local zoom in Figure 18a. The stack's power undershoot was less than 4 kW, and the range of power fluctuation was less than ±1 kW. Figure 18b shows the current response curve during the de-loading stage, and Figure 18c shows the voltage response curve during the de-loading stage. Overall, the transient response of

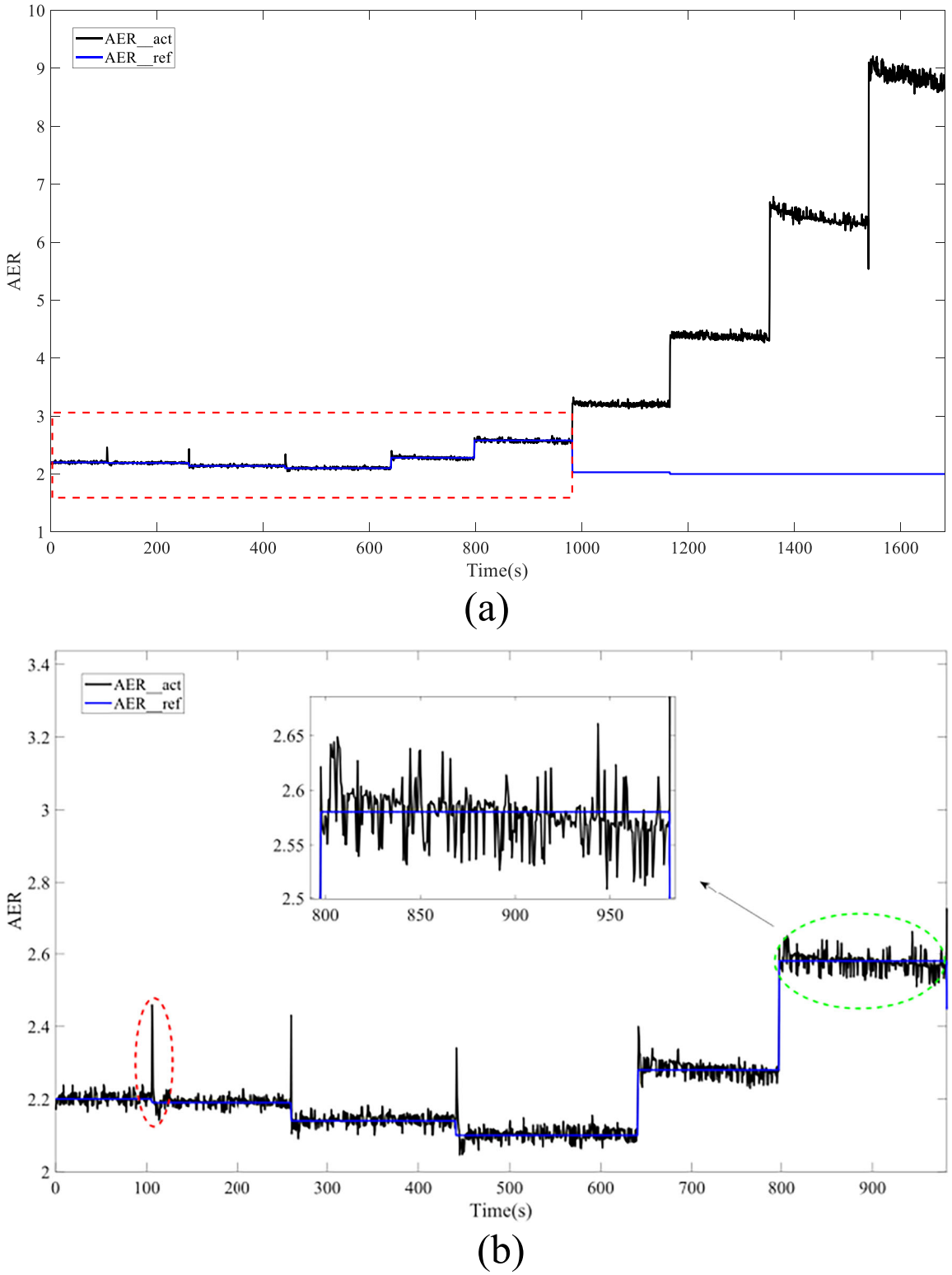

FIGURE 22 | Full-stage and high-power stage AER. (a) Actual AER versus reference AER in the de-loading stage. (b) Actual AER versus reference AER at high power.

the current and voltage of the stack, as well as the steady-state stability, are reasonable.

Figure 19a contrasts the engine load and the system power output. It is evident that the system output power steadily changed as the load changed. The maximum overshoot happened during the sudden load change from 86 kW to 77 kW (as shown in the local zoomed-in figure in Figure 19a), where the overshoot was less than 3 kW. When the load was 77 kW, the system output power fluctuated more drastically, with an average deviation of 0.7 kW. Figure 19b,c present the high-voltage and low-voltage auxiliary power in the de-loading stage. In Figure 19b,c, the power fluctuation range of the auxiliary components under different loads is very small, and there is

only a short power undershoot, followed by a quick recovery of stable operation.

The contrast of the reference and actual air flow during the de-loading stage is shown in Figure 20. The findings demonstrate that the airflow rate swiftly and steadily followed the reference value in both transient and steady states. When the load was 86 kW, the air mass flow rate during steady-state conditions had the most significant fluctuation (as shown in the enlarged red ellipse in Figure 20), and the deviation value was less than 3 g/s. In addition, the air flow rate undershot by 7 g/s, the maximum value of the undershoot in the whole de-loading stage, and reached the reference value within 5 s (as shown in Figure 21).

Figure 22a shows the actual AER during the de-loading stage compared to the reference value. The actual AER was large at low power due to the minimum air flow limitations, so that the focus would be on the larger power (86–41 kW) process (i.e., the portion of the red box in Figure 22a). Figure 22b shows an enlarged view of the red-boxed portion of Figure 22a. In Figure 22b, the actual AER can follow the reference value stably. The green ellipse part is the process of the de-loading stage, where the actual AER fluctuated most significantly, and the steady-state error was less than 0.15.

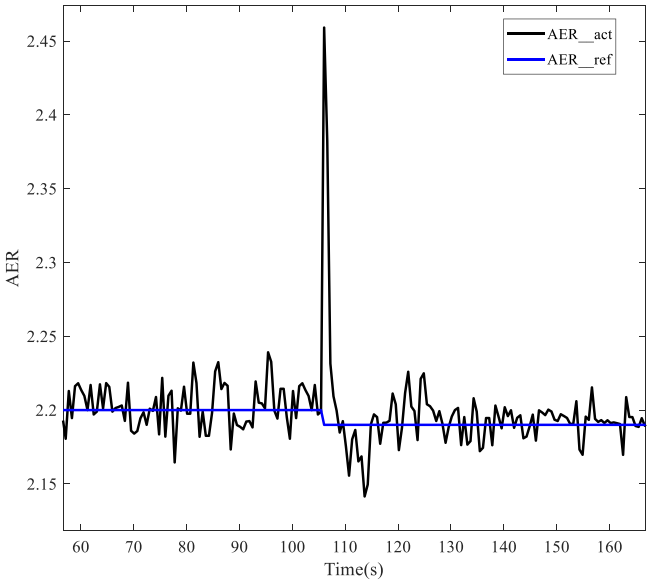

FIGURE 23 | Enlarged view of the red oval portion of Figure 21b.

It is also found in Figure 23 that there were transient increases and undershooting of the AER during the regulation process. Due to the air compressor's delayed response, the reference air flow rate dropped when the load suddenly changed, but the actual air flow rate did not fall instantly. Therefore, the actual air supply was much higher than the air consumption, resulting in an instantaneous increase in the AER. Due to the large feedback deviation, the air flow rate reduced rapidly and substantially, resulting in a large undershoot, followed by rapid adjustment to the reference value.

The contrast between the reference and actual air pressure under the de-loading stage is depicted in Figure 24. Overall, the actual air pressure followed the reference air pressure well during the steady-state operation with different loads, and the average pressure deviation was less than ±1 kPa. At the same time, the transient process pressure undershoots decreased gradually with the reduction of the load (the maximum undershoot was 15 kPa), and no obvious undershoot occurred with a smaller load (9–41 kW). In addition, the actual air pressure during the de-load stage could reach the reference value within 8 s (as shown in the partial enlargement in Figure 24) and followed the reference pressure stably.

Figure 25 shows the dynamic change curves of the average and minimum single-cell voltages in the de-loading stage. It is evident that when the system power decreased, the single-cell voltage progressively rose. Meanwhile, the fluctuation range of single-cell average voltage was minimal when the fuel cell operated steadily under different loads.

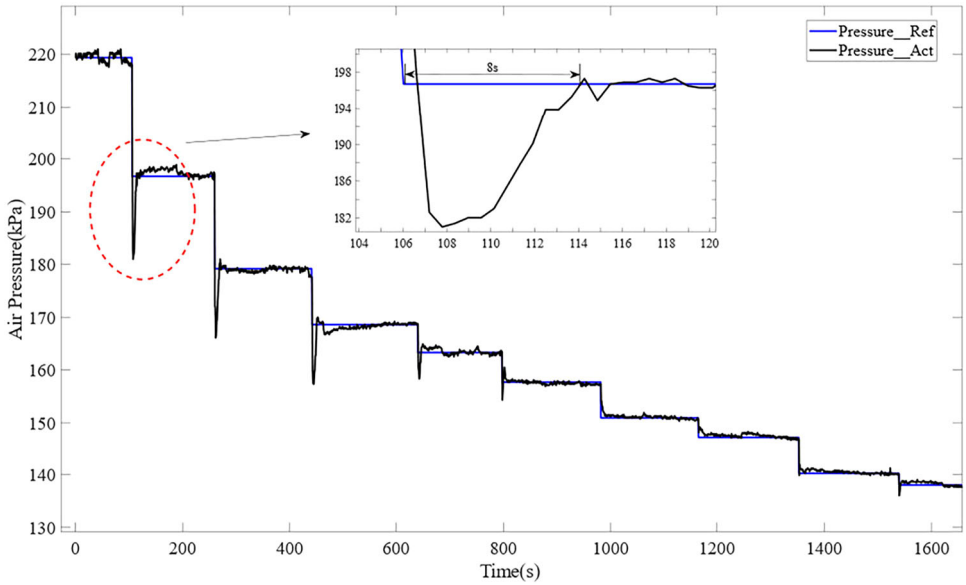

FIGURE 24 | Comparison of actual air pressure and reference air pressure in the de-loading stage.

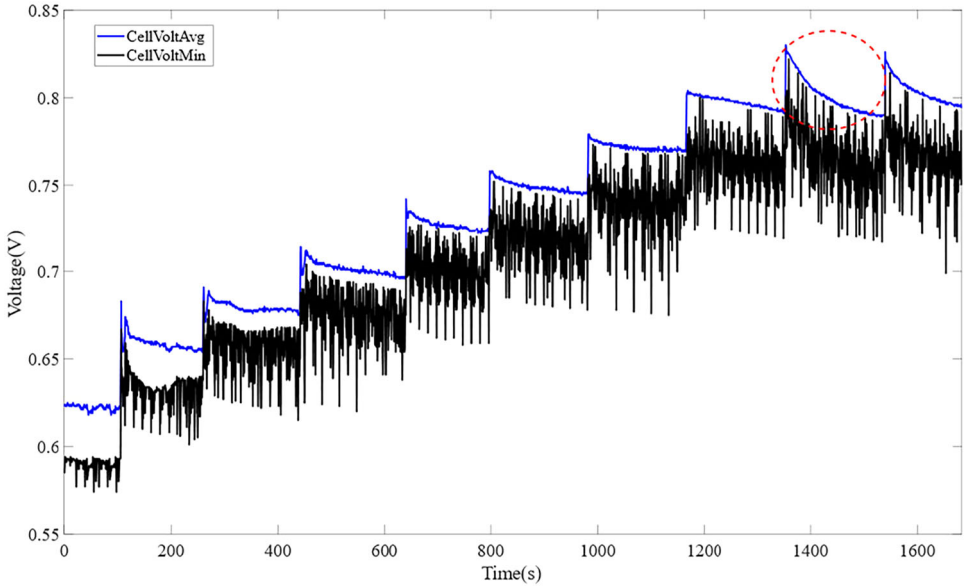

FIGURE 25 | Dynamic change graphs for a single cell's average and lowest voltage in the de-loading stage.

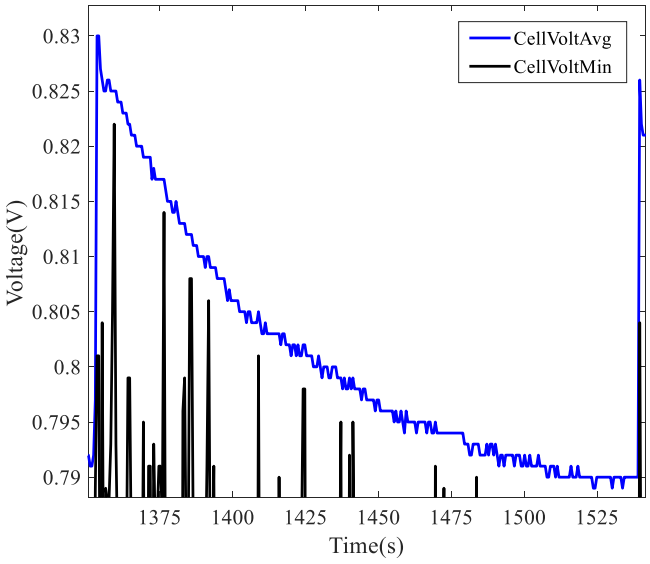

FIGURE 26 | Enlarged view of the red oval portion.

Less than 0.045 V separated the fuel cell's average single-cell voltage's highest and minimum values (shown in Figure 26), which illustrates the stability of the single-cell operation. The distribution range of the single cell's lowest and average voltage difference is displayed in Figure 27. It can be seen that most voltage differences are below 0.05 V, and the maximum is smaller than 0.1 V, indicating that a single cell's average and minimum voltage differed just slightly. It also shows that single-cell consistency was better, and the control strategy could lead the system to operate stably in a de-loading state.

4.3 | Wide Range of Sudden Load Drop Stage

It is clear from the discussion in Section 4.2 that controlling air state variables in both transient and steady states at various engine loads was suitable in the system's de-loading stage. Due to current limitations, the control strategy was also superior in this stage. Therefore, to further illustrate the capability of the air supply system controller, this section explores the effects of transient and steady-state control during a wide range of sudden load drops.

As shown in Figure 28, the engine load suddenly dropped from 86 kW to 5 kW. Figure 29 shows the contrast between the system's power output and the load. The output power fluctuates slightly during the 86 kW and 5 kW steady-state operation, with a fluctuation range of ± 0.3 kW. The transient undershoots were effectively constrained to within 1 kW, achieving regulation within 5.2 s, which demonstrates the system's exceptional load-tracking capability and robust dynamic performance [43–45].

The contrast of the reference and actual air mass flow rates during a variety of abrupt load drops is shown in Figure 30a. The actual value followed the reference value well, without significant undershoot during the transient response. The enlarged plot in Figure 30a shows that it dropped to the minimum value during the transient process and recovered quickly, reaching the reference value within 6 s. The difference between the reference and actual value under various abrupt load drops is depicted in Figure 30b. It can be found that only in the transient process did the actual value of the air flow rate differ from the reference value. Then, the deviation decreased rapidly, and the average deviation in the steady-state operation process was 0.86 g/s.

The contrast of the reference and actual pressure throughout a wide range of abrupt load drops is shown in Figure 31a. It is evident that under steady-state operation, the real air pressure might more closely resemble the reference air pressure. From the local zoom in Figure 31a, it is evident that the transient process's air pressure undershoot was 11.7 kPa, and the response time was 13 s. Figure 31b displays the distribution of the variation among the air pressure's actual value and its reference value across the range. The average deviation during the process was 2.2 kPa, and the average deviation of air pressure

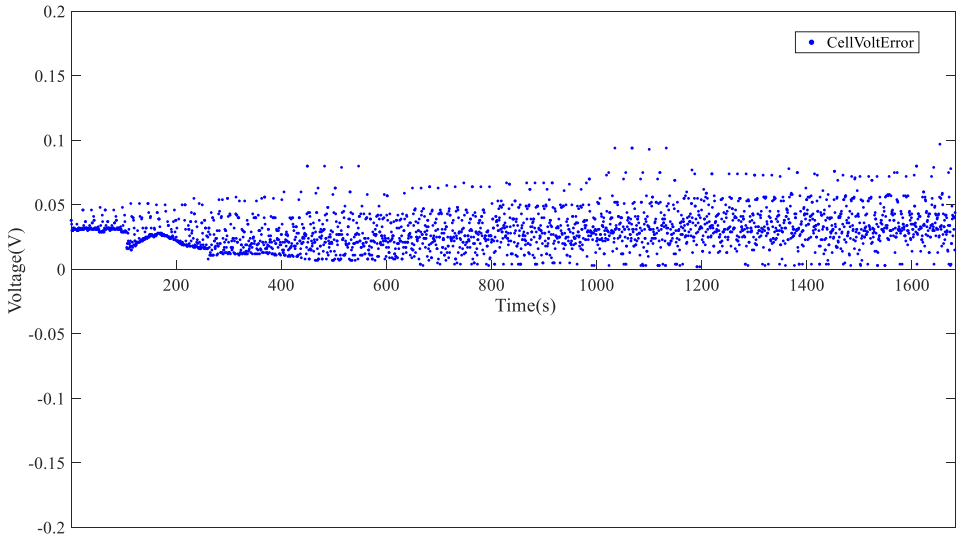

FIGURE 27 | Variation among the single cell's minimum and average voltage in the de-loading stage.

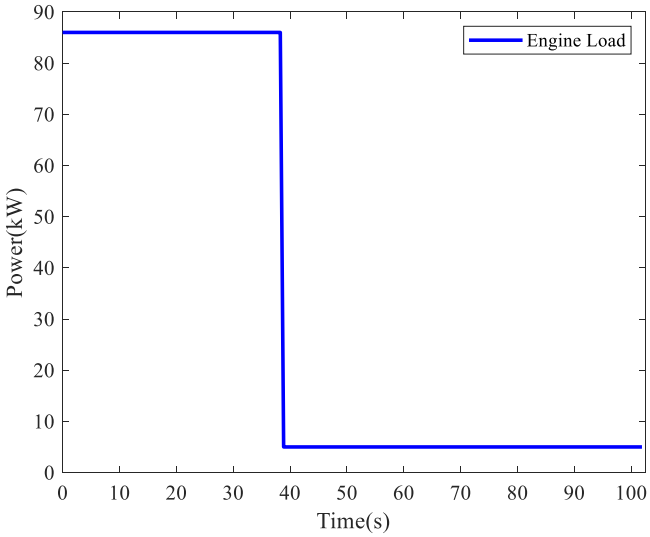

FIGURE 28 | Engine load of sudden load drop.

during steady-state operation was 1.6 kPa. It can be seen that the wide range of load changes had a more pronounced effect on air flow and pressure. According to the overall testing findings, the air supply system controller suggested in this article has enough capacity to fulfil the demands throughout a wide range of abrupt power drops.

5 | Conclusions

This manuscript presents the implementation and analysis of a feed-forward PID-based air mass flow and pressure control strategy for an 86 kW fuel cell engine. Experimental investigations were conducted to evaluate the fuel cell system's power output and air dynamics under varying load conditions. The main conclusions are as follows:

1. During the loading and de-loading stages, the system's power output reliably tracked the engine load under steady-state conditions. Due to current rise limitations, the loading stage exhibited an extended regulation time in transient scenarios. However, this also contributed to the system's transient stability, resulting in minimal overshoot. Conversely, transient undershoots diminished progressively during the de-loading stage, and the regulation time was reduced. Furthermore, the system's auxiliary components, including high-voltage and low-voltage auxiliaries, operated stably across different load conditions.
2. The system demonstrated the capability to maintain steady power output following sudden load drops over a wide range. The fluctuation in system output power during steady-state operation was confined to ±0.3 kW. Transient undershoots were kept below 1 kW, with a regulation time of 5.2 s, indicating the system's robust ability to track load changes effectively.
3. The air mass flow rate exhibited a consistent tracking response across varying loads, with an average flow rate deviation of 1.6 g/s, a maximum deviation of 4 g/s, and a maximum response time of 12.5 s. Pressure deviation remained within a fluctuation range of ±1.82 kPa, with a maximum deviation of 11.7 kPa and a maximum regulation time of 15 s, all within acceptable limits for engine operation. However, static models for the intercooler and humidifier are adopted, ignoring dynamic response delays of thermal and humidity changes, thus affecting control precision. And experimental validation is limited to steady-state and step load conditions, while extreme environmental temperatures and long-term variable load cycles are not covered in this study.
4. The dynamic response of a single cell's average and minimum voltages during load changes demonstrated the system's stable operational capability under diverse conditions. The voltage difference between the average and minimum values was predominantly less than 0.05 V, highlighting the high consistency among

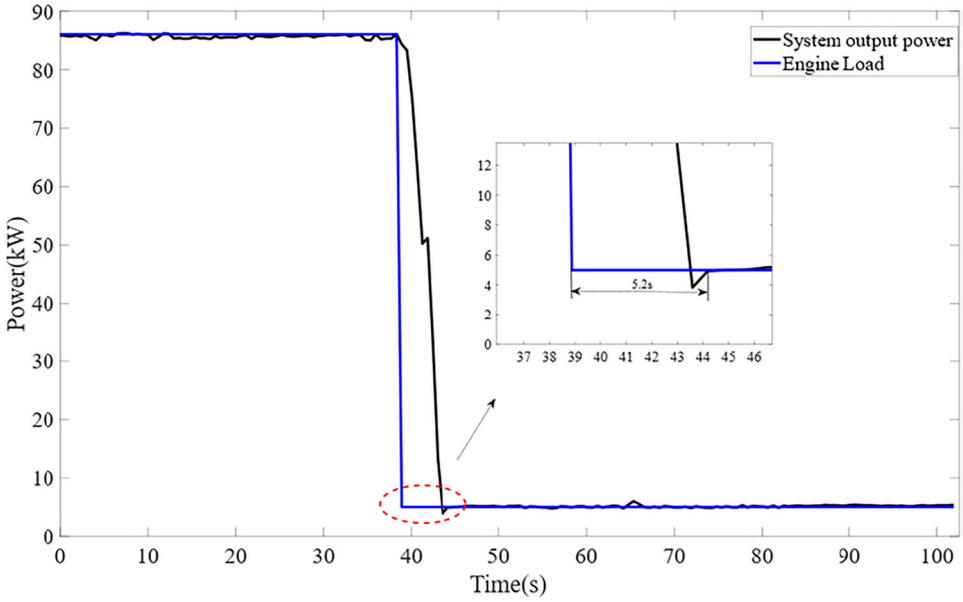

FIGURE 29 | System output power versus engine load of sudden load drop.

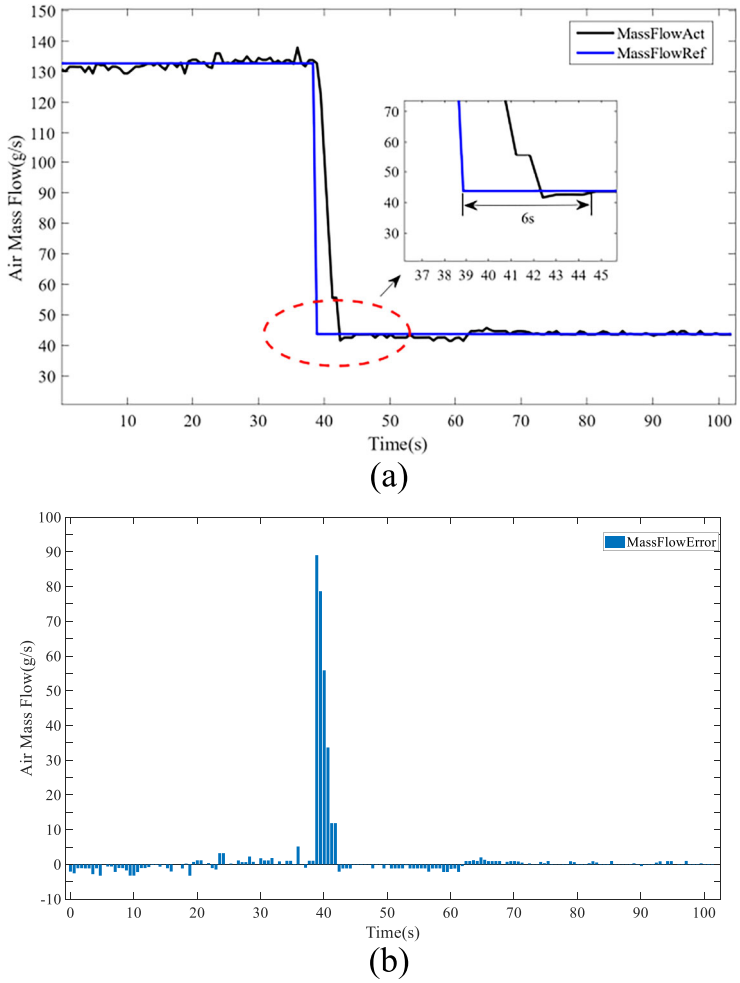

FIGURE 30 | Comparison of air flow values and differences under different conditions. (a) Actual air flow versus reference air flow of sudden load drop. (b) Difference between actual air flow and reference air flow of sudden load drop.

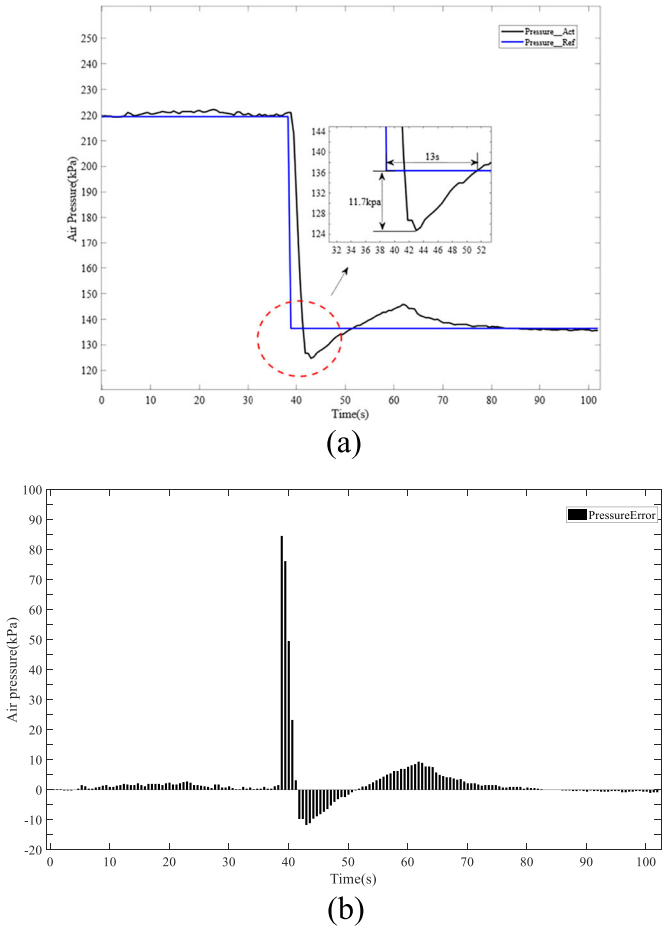

FIGURE 31 | Comparison of air pressure values and differences under different conditions. (a) Actual air pressure versus reference air pressure of sudden load drop. (b) Difference between actual air pressure and reference air pressure of sudden load drop.

individual cells, which is crucial for ensuring the longevity and reliability of the fuel cell stack.

5. Due to the limitations of the experimental conditions, this study calculated the change in air humidity using a static humidifier model, which could not capture the dynamic hydration effect. A transient humidity sensor would be built into the PEMFC system in the future. The effects of humidity on stacking performance will be quantified by parameters such as membrane hydration and conductivity.

Acknowledgements

This study is Supported by the National Natural Science Foundation of China (Grants U23A20680), Jiangsu Province Carbon Peaking and Carbon Neutrality Science, Technology Innovation Special Fund (Industry Foresight and Key Technology Core Research) Project (BE2023091-2), Provincial Science and Technology Innovation Strategy Special Project of Shaoguan City (230317166277914), Special Program for Science and Technology Innovation in Industrial Bases (2023010402010790).

References

1. M. Amin, H. H. Shah, A. G. Fareed, et al., "Hydrogen Production Through Renewable and Non-Renewable Energy Processes and Their Impact on Climate Change," *International Journal of Hydrogen Energy* 47 (2022): 33112–33134, https://doi.org/10.1016/j.ijhydene.2022.07.172.

2. M. Wang, G. Wang, Z. Sun, Y. Zhang, and D. Xu, "Review of Renewable Energy-Based Hydrogen Production Processes for Sustainable Energy Innovation," *Global Energy Interconnection* 2 (2019): 436–443, https://doi.org/10.1016/j.gloei.2019.11.019.

3. J. Mei, X. Meng, X. Tang, et al., "An Accurate Parameter Estimation Method of the Voltage Model for Proton Exchange Membrane Fuel Cells," *Energies* 17 (2024): 2917, https://doi.org/10.3390/en17122917.

4. X. Li, T. Ye, X. Meng, et al., "Advances in the Application of Sulfonated Poly(Ether Ether Ketone) (Speek) and Its Organic Composite Membranes for Proton Exchange Membrane Fuel Cells (Pemfcs)," *Polymers* 16 (2024): 2840, https://doi.org/10.3390/polym16192840.

5. T. L. Oladosu, J. Pasupuleti, T. S. Kiong, S. P. J. Koh, and T. Yusaf, "Energy Management Strategies, Control Systems, and Artificial Intelligence-Based Algorithms Development for Hydrogen Fuel Cell-Powered Vehicles: A Review," *International Journal of Hydrogen Energy* 61 (2024): 1380–1404, https://doi.org/10.1016/j.ijhydene.2024.02.284.

6. Y. Wang, D. F. Ruiz Diaz, K. S. Chen, Z. Wang, and X. C. Adroher, "Materials, Technological Status, and Fundamentals of PEM Fuel Cells – A Review," *Materials Today* 32 (2020): 178–203, https://doi.org/10.1016/j.mattod.2019.06.005.

7. X. Meng, C. Sun, J. Mei, et al., "Fuel Cell Life Prediction Considering the Recovery Phenomenon of Reversible Voltage Loss," *Journal of Power Sources* 625 (2025): 235634, https://doi.org/10.1016/j.jpowsour.2024.235634.

8. X. Meng, J. Mei, X. Tang, J. Jiang, C. Sun, and K. Song, "The Degradation Prediction of Proton Exchange Membrane Fuel Cell Performance Based on a Transformer Model," *Energies* 17 (2024): 3050, https://doi.org/10.3390/en17123050.

9. D. Hu, L. Hu, J. Wang, J. Li, and Q. Yang, “Stability Enhancement Optimization Method for Suppressing Speed Fluctuation Under Large-Scale Speed Regulation Process of Super-High-Speed Electric Air Compressor,” *Nonlinear Dynamics* 105 (2021): 1581–1592, https://doi.org/10.1007/s11071-021-06678-8.

10. Y. Li, Z. Hu, H. Liu, et al., “Comprehensive Analysis of Cathode Air Pressure of Fuel Cell Powertrain System of Aircraft: Performance, Efficiency, and Control,” *Energy Conversion and Management* 283 (2023): 116903, https://doi.org/10.1016/j.enconman.2023.116903.

11. H. Chen, Z. Liu, X. Ye, L. Yi, S. Xu, and T. Zhang, “Air Flow and Pressure Optimization for Air Supply in Proton Exchange Membrane Fuel Cell System,” *Energy* 238 (2022): 121949, https://doi.org/10.1016/j.energy.2021.121949.

12. J.-K. Kuo, U. Thamma, A. Wongcharoen, and Y.-K. Chang, “Optimized Fuzzy Proportional Integral Controller for Improving Output Power Stability of Active Hydrogen Recovery 10-kW Pem Fuel Cell System,” *International Journal of Hydrogen Energy* 50 (2024): 1080–1093, https://doi.org/10.1016/j.ijhydene.2023.08.364.

13. X. Ye, T. Zhang, and Y. Liu, “Cathode Gas Pressure and Mass Flow Rate Closed—Loop Control in Fuel Cell System,” *Automobile Technology* 6 (2022): 14–19, https://doi.org/10.19620/j.cnki.1000-3703.20211259.

14. A. Shen and Y. Zhan, “RBF-PID Control of Fuel Cell Oxygen Excess Radio Based on Secondary Performance Index,” *Information and Control* 50 (2021): 498–504,512, https://doi.org/10.13976/j.cnki.xk.2021.0407.

15. Z. Baroud, M. Benmiloud, A. Benalia, and C. Ocampo-Martinez, “Novel Hybrid Fuzzy-PID Control Scheme for Air Supply in Pem Fuel-Cell-Based Systems,” *International Journal of Hydrogen Energy* 42 (2017): 10435–10447, https://doi.org/10.1016/j.ijhydene.2017.01.014.

16. J. Pan, Z. Liu, and Y. Ding, “Study on a Control Method of PEMFC Air Transmission System,” *Acta Energiae Solaris Sinica* 41 (2020): 172–177, https://doi.org/10.19912/j.0254-0096.2020.04.025.

17. A. Routh, S. Ghosh, I. Dey, M. Rahaman, and A. Ghosh, “Optimization of PEMFC Pressure Control Using Fractional Pi/D Controller With Non-Integer Order: Design and Experimental Evaluation,” *Engineering Research Express* 6 (2024): 025001, https://doi.org/10.1088/2631-8695/ad33ff.

18. A. Routh, S. Ghosh, M. Rahaman, and A. Ghosh, “Fractional Pi^{Λ} D^{M} Controller Design for Non-Linear PEM Fuel Cell for Pressure Control Based on a Genetic Algorithm,” *Indian Chemical Engineer* 65 (2023): 125–142, https://doi.org/10.1080/00194506.2022.2133641.

19. J. Han, S. Yu, and S. Yi, “Adaptive Control for Robust Air Flow Management in An Automotive Fuel Cell System,” *Applied Energy* 190 (2017): 73–83, https://doi.org/10.1016/j.apenergy.2016.12.115.

20. C.-Y. Chuang, C.-H. Lan, T.-S. Lan, X.-J. Dai, and J.-H. Qin, “Flow Control of Proton Exchange Membrane Fuel Cell With Theory of Inventive Problem Solving (Triz),” *Sensors and Materials* 33 (2021): 1603–1617, https://doi.org/10.18494/SAM.2021.3176.

21. A. Pilloni, A. Pisano, and E. Usai, “Observer-Based Air Excess Ratio Control of a PEM Fuel Cell System via High-Order Sliding Mode,” *IEEE Transactions on Industrial Electronics* 62 (2015): 5236–5246, https://doi.org/10.1109/TIE.2015.2412520.

22. Z. Liu, J. Chen, H. Chen, and C. Yan, “Air Supply Regulation for PEMFC Systems Based on Uncertainty and Disturbance Estimation,” *International Journal of Hydrogen Energy* 43 (2018): 11559–11567, https://doi.org/10.1016/j.ijhydene.2018.01.189.

23. P. Wang, Y. Ma, J. Li, Y. Gao, Y. Zhang, and D. Ma, “A Novel Control Algorithm of the Air Supply Subsystem: Based on Dynamic Modeling of Proton Exchange Membrane Fuel Cell,” *Processes* 10 (2022): 1499, https://doi.org/10.3390/pr10081499.

24. H. Li, C. Sun, J. Li, et al., “Self-Tuning Oxygen Excess Ratio Control for Proton Exchange Membrane Fuel Cells Under Dynamic Conditions,” *Processes* 12 (2024): 2807, https://doi.org/10.3390/pr12122807.

25. S. Fang, J. Feng, X. Fan, D. Chen, and C. Tan, “Dual-Sliding-Surface Robust Control for the PEMFC Air-Feeding System Based on Terminal Sliding Mode Algorithm,” *Actuators* 13 (2024): 459, https://doi.org/10.3390/act13110459.

26. Y. Wang, Y. Wang, J. Xu, and T. Chai, “Observer-Based Discrete Adaptive Neural Network Control for Automotive Pemfc Air-Feed Subsystem,” *IEEE Transactions on Vehicular Technology* 70 (2021): 3149–3163, https://doi.org/10.1109/TVT.2021.3064604.

27. H. Deng, Q. Li, W. Chen, and G. Zhang, “High-Order Sliding Mode Observer Based Oer Control for PEM Fuel Cell Air-Feed System,” *IEEE Transactions on Energy Conversion* 33 (2018): 232–244, https://doi.org/10.1109/TEC.2017.2742144.

28. L. Wei, X. Zhu, X. Wang, Z. Hu, and M. Wang, “Research on the Coordinated Control of Oxygen Excess Ratio and Air Pressure for Pemfc's Air Supply System,” *International Journal of Hydrogen Energy* 69 (2024): 122–133, https://doi.org/10.1016/j.ijhydene.2024.04.361.

29. E. Bacher-Chong, M. A. Ayubirad, Z. Qiu, H. Wang, A. Goshtasbi, and H. R. Ossareh, “Hierarchical Fuel-Cell Airpath Control: An Efficiency-Aware Mimo Control Approach Combined With a Novel Constraint-Enforcing Reference Governor,” *IEEE Transactions on Control Systems Technology* 32 (2024): 534–549, https://doi.org/10.1109/TCST.2023.3329909.

30. Z. Liu, H. Chen, L. Peng, X. Ye, S. Xu, and T. Zhang, “Feedforward-Decoupled Closed-Loop Fuzzy Proportion-Integral-Derivative Control of Air Supply System of Proton Exchange Membrane Fuel Cell,” *Energy* 240 (2022): 122490, https://doi.org/10.1016/j.energy.2021.122490.

31. F. Chen and X. Chen, “Internal Model Decoupling Controller Design for High Pressure PEMFC Air Supply System,” *Journal of Tong Ji University (Natural Science)* 44 (2016): 1924–1930, https://doi.org/10.11908/j.issn.0253-374x.2016.12.017.

32. D. Song, F. Zeng, X. Zeng, and Q. Wu, “Research on Dynamic Decoupling Control of Air Supplying Loop In Fuel Cell System Based on Pressure Compensation,” *Journal of Mechanical Science and Technology* 35 (2021): 2677–2688, https://doi.org/10.1007/s12206-021-0538-8.

33. Y. Li, P. Pei, Z. Ma, P. Ren, and H. Huang, “Method for System Parameter Identification and Controller Parameter Tuning for Super-Twisting Sliding Mode Control in Proton Exchange Membrane Fuel Cell System,” *Energy Conversion and Management* 243 (2021): 114370, https://doi.org/10.1016/j.enconman.2021.114370.

34. T. Sun, X. Zhang, B. Chen, and X. Liu, “Coordination Control Strategy for the Air Management of Heavy Vehicle Fuel Cell Engine,” *International Journal of Hydrogen Energy* 45 (2020): 20360–20368, https://doi.org/10.1016/j.ijhydene.2019.10.134.

35. B. Wang, X. Zhao, L. Quan, Y. Li, Y. Hao, and L. Ge, “A Method for Improving Flow Control Valve Performance Based on Active Differential Pressure Regulation,” *Measurement* 219 (2023): 113271, https://doi.org/10.1016/j.measurement.2023.113271.

36. M. Zhao, W. Wang, X. Zhu, et al., “Simulation and Control Strategy Study of the Hydrogen Supply System of a Fuel Cell Engine,” *Energies* 16 (2023): 4931, https://doi.org/10.3390/en16134931.

37. I. Darjat, I. Sulistyo, A. Triwiyatno, Sudjadi, and A. Kurniahadi, “Designing Hydrogen and Oxygen Flow Rate Control on a Solid Oxide Fuel Cell Simulator Using the Fuzzy Logic Control Method,” *Processes* 8 (2020): 154–177, https://doi.org/10.3390/pr8020154.

38. C. Li, H. Zhao, H. Liu, et al., “Gas Supply Control and Experimental Validation for Polymer Electrolyte Membrane Fuel Cells,” *Mechatronics* 91 (2023): 102958, https://doi.org/10.1016/j.mechatronics.2023.102958.

39. D. Zhao, L. Xu, Y. Huangfu, M. Dou, and J. Liu, “Semi-Physical Modeling and Control of a Centrifugal Compressor for the Air Feeding of a Pem Fuel Cell,” *Energy Conversion and Management* 154 (2017): 380–386, https://doi.org/10.1016/j.enconman.2017.11.030.

40. F. Duan and Z. Kang, "Oxygen Excess Ratio Feedforward Control Based on Eso for PEMFC in Dc Off-Grid Hydrogen Production Systems," *International Journal of Hydrogen Energy* 77 (2024): 347–358, https://doi.org/10.1016/j.ijhydene.2024.06.069.

41. Z. Liu, L. Liu, and Y. Zhou, "Modelling and Simulation Analysis of Closed Proton Exchange Membrane Fuel Cell System," *Energy Reports* 8 (2022): 162–168, https://doi.org/10.1016/j.egyr.2021.11.033.

42. A. Kiam Heong Ang, G. Chong, and Li Yun Li, "PID Control System Analysis, Design, and Technology," *IEEE Transactions on Control Systems Technology* 13 (2005): 559–576, https://doi.org/10.1109/TCST.2005.847331.

43. Z. Liu, B. Zhang, and S. Xu, "Research on Air Mass Flow-Pressure Combined Control and Dynamic Performance of Fuel Cell System for Vehicles Application," *Applied Energy* 309 (2022): 118446, https://doi.org/10.1016/j.apenergy.2021.118446.

44. Z. Liu, H. Chen, and T. Zhang, "Analysis and Optimization of Dynamic Response During the Startup Process of Proton Exchange Membrane Fuel Cell," *Journal of Power Sources* 628 (2025): 235904, https://doi.org/10.1016/j.jpowsour.2024.235904.

45. X. Yang, P. Tan, L. Fang, et al., "Dynamic Performance and Potential Failure Analysis of PEMFC System Without External Humidifier Based on Real Vehicle Testing," *International Journal of Hydrogen Energy* 138 (2025): 648–659, https://doi.org/10.1016/j.ijhydene.2025.05.244.